

## CHARACTERIZING SIGNAL LOSS, ERROR, AND BIAS IN THE 21CM REIONIZATION POWER SPECTRUM: A REVISED STUDY OF PAPER-64

CARINA CHENG<sup>1,◇</sup>, AARON R. PARSONS<sup>1,2</sup>, MATTHEW KOLOPANIS<sup>3</sup>, DANIEL C. JACOBS<sup>3</sup>, SAUL A. KOHN<sup>4</sup>, ADRIAN LIU<sup>1,5,†</sup>,  
 JONATHAN C. POBER<sup>6</sup>, JAMES E. AGUIRRE<sup>4</sup>, ZAKI S. ALI<sup>1</sup>, GIANNI BERNARDI<sup>7,8,9</sup>, RICHARD F. BRADLEY<sup>10,11,12</sup>, CHRIS L.  
 CARILLI<sup>13,14</sup>, DAVID R. DEBOER<sup>2</sup>, MATTHEW R. DEXTER<sup>2</sup>, JOSHUA S. DILLON<sup>1,\*</sup>, PAT KLIMA<sup>11</sup>, DAVID H. E. MACMAHON<sup>2</sup>,  
 DAVID F. MOORE<sup>4</sup>, CHUNEETA D. NUNHOKEE<sup>8</sup>, WILLIAM P. WALBRUGH<sup>7</sup>, ANDRE WALKER<sup>7</sup>

<sup>1</sup>Astronomy Dept., U. California, Berkeley, CA

<sup>2</sup>Radio Astronomy Lab., U. California, Berkeley CA

<sup>3</sup>School of Earth and Space Exploration, Arizona State U., Tempe AZ

<sup>4</sup>Dept. of Physics and Astronomy, U. Penn., Philadelphia PA

<sup>5</sup>Berkeley Center for Cosmological Physics, Berkeley, CA

<sup>6</sup>Dept. of Physics, Brown University, Providence RI

<sup>7</sup>Square Kilometer Array, S. Africa, Cape Town South Africa

<sup>8</sup>Dept. of Physics and Electronics, Rhodes University, South Africa

<sup>9</sup>INAF-Instituto di Radioastronomia, Bologna Italy

<sup>10</sup>Dept. of Electrical and Computer Engineering, U. Virginia, Charlottesville VA

<sup>11</sup>National Radio Astronomy Obs., Charlottesville VA

<sup>12</sup>Dept. of Astronomy, U. Virginia, Charlottesville VA

<sup>13</sup>National Radio Astronomy Obs., Socorro NM

<sup>14</sup>Cavendish Lab., Cambridge UK

### ABSTRACT

The Epoch of Reionization (EoR) is an uncharted era in our Universe’s history during which the first stars and galaxies led to the ionization of neutral hydrogen in the intergalactic medium. There are many experiments investigating the EoR by tracing the 21 cm line of neutral hydrogen, a signal which is very faint and difficult to isolate. With a new generation of instruments and a statistical power spectrum detection in our foreseeable future, it has become increasingly important to develop techniques that help maximize sensitivity while validating results. Additionally, it is imperative to understand the trade-offs between different methods and their effects on power spectrum estimates. In this paper, we focus on three major themes — signal loss, power spectrum error estimation, and bias in measurements. We describe techniques that affect these themes using both toy models and data taken by the 64-element configuration of the Donald C. Backer Precision Array for Probing the Epoch of Reionization (PAPER). In particular, we highlight how detailed investigations of these themes have led to a revised, higher 21 cm power spectrum upper limit from PAPER-64. This revised result mostly stems from an improved signal loss calculation for loss associated with empirically estimated covariances and supersedes results from previously published PAPER analyses.

### 1. INTRODUCTION

By about one billion years after the Big Bang ( $z \sim 6$ ), the first stars and galaxies are thought to have ionized all the neutral hydrogen that dominated the baryonic matter content in the Universe. This transition period, during which the first luminous structures formed from gravitational collapse and began to emit intense radia-

tion that ionized the cold neutral gas into a plasma, is known as the Epoch of Reionization (EoR). The EoR is a relatively unexplored era in our *cosmic dawn*, which spans from the birth of the first stars to the full reionization of the intergalactic medium (IGM). Its history encodes important information regarding the nature of the first galaxies and the processes of structure formation. Direct measurements of the EoR would unlock powerful characteristics about the IGM, revealing connections between the matter distribution exhibited via cosmic microwave background (CMB) studies and the highly structured web of galaxies we observe today (for a review, see [Furlanetto et al. 2006](#)).

One promising technique to probe the EoR is to tar-

◇[ccheng@berkeley.edu](mailto:ccheng@berkeley.edu)

†Hubble Fellow

\*NSF AAPF Fellow

get the 21 cm wavelength signal that is emitted and absorbed by neutral hydrogen via its spin-flip transition (Furlanetto et al. 2006; Morales & Wyithe 2010; Pritchard & Loeb 2012). This tomography technique is powerful because it can be observed both spatially and as a function of redshift — that is, the wavelength of the signal reaching our telescopes can be directly mapped to a distance from where the emission originated before stretching out as it traveled through expanding space. Tracing the 21 cm line as a function of redshift offers a window into the evolution of ionization, temperature, and density fluctuations.

Although a detection of the EoR remains elusive, there are several radio telescope experiments that have succeeded in using the 21 cm signal from hydrogen to place constraints on the brightness of the signal. Examples of experiments investigating the mean brightness temperature of the EoR relative to the CMB are the Experiment to Detect the Global EoR Signature (EDGES; Bowman & Rogers 2010), the Large Aperture Experiment to Detect the Dark Ages (LEDA; Bernardi et al. 2016), the Dark Ages Radio Explorer (DARE; Burns et al. 2012), the Sonda Cosmológica de las Islas para la Detección de Hidrógeno Neutro SciHi (SCI-HI; Voytek et al. 2014), the Broadband Instrument for Global Hydrogen Reionization Signal (BIGHORNS; Sokolowski et al. 2015), and the Shaped Antenna measurement of the background Radio Spectrum (SARAS; Patra et al. 2015). Radio interferometers which seek to measure statistical power spectra include the Giant Metre-wave Radio Telescope (GMRT; Paciga et al. 2013), the LOw Frequency Array (LOFAR; van Haarlem et al. 2013), the Murchison Widefield Array (MWA; Tingay et al. 2013), the 21 Centimeter Array (21CMA; Peterson 2004; Wu 2009), and PAPER (Parsons et al. 2010). The Hydrogen Epoch of Reionization Array (HERA), which is currently being built, is a next-generation instrument that aims to combine lessons learned from previous experiments and is forecast to be able to make a high-significance power spectrum detection with an eventual 350 elements using current analysis techniques (Pober et al. 2014; Liu & Parsons 2016; ?; DeBoer et al. 2017).

The major challenge that faces all 21 cm experiments is isolating a small signal that is buried underneath foregrounds and instrumental systematics that are, when combined, four to five orders of magnitude brighter (e.g., Santos et al. 2005; Ali et al. 2008; de Oliveira-Costa et al. 2008; Jelić et al. 2008; Bernardi et al. 2009, 2010; Ghosh et al. 2011; Pober et al. 2013; Dillon et al. 2014; Kohn et al. 2016). A clean measurement therefore requires an intimate understanding of the instrument and a rigorous study of data analysis choices. With continual progress being made in the field and HERA on the horizon, it is becoming increasingly important to understand how the methods we choose interact with each other to affect power spectrum results. More specifically, it is imperative to develop techniques and tests that ensure the accuracy and reliability of a potential EoR detection. In

this paper, we discuss three topics that are essential to investigate for a robust 21 cm power spectrum analysis. We also highlight four power spectrum techniques and their trade-offs, potential pitfalls, and connections to the themes. We first approach the themes from a broad perspective, and then perform a detailed case study using data from the 64-element configuration of PAPER, motivating a revised PAPER-64 power spectrum from the lessons learned.

This paper is organized into two main sections. In Section 2 we introduce the three themes of our focus, using a toy model to develop intuition for each one. In Section 3 we present a case study into each theme using data from the PAPER-64 array, highlighting key changes from the previously published result in Ali et al. (2015), henceforth known as A15, which have led to a revised PAPER-64 power spectrum result (Kolopanis et al., *in prep*). We conclude in Section 4.

## 2. POWER SPECTRUM THEMES AND TECHNIQUES

There are many choices a 21 cm data analyst must consider. How can time-ordered measurements be combined? How can the variance of the data be estimated? In what way(s) can the data be weighted to suppress contaminated modes while not destroying an EoR signal? How can a statistically significant detection of a signal be properly identified? Many common techniques, such as averaging data, weighting, bootstrapping, and jackknife testing, address these issues but harbor additional trade-offs. For example, an aggressive filtering method may succeed in eliminating interfering systematics but comes at the cost of losing some EoR signal. A chosen weighting scheme may maximize sensitivity but fail to suppress foregrounds.

Though there are many data analysis choices, measuring the statistical 21 cm power spectrum ultimately requires robust methods for determining accurate confidence intervals and rigorous techniques to identify and control systematics. In this paper, we focus on three 21 cm power spectrum themes that encapsulate this goal and discuss four techniques that interplay with each other and impact the themes. We will give brief definitions now, and build intuition for each theme in the sections to follow.

### Power Spectrum Themes

A deep understanding of the following three themes is essential for the accuracy and interpretation of a 21 cm power spectrum result. Stemming from a re-analysis of PAPER-64 data, we believe these themes serve as an important checklist for a rigorous power spectrum analysis.

- **Signal Loss** (Section 2.1): Signal loss refers to attenuation of the target cosmological signal in a power spectrum estimate. Certain analysis techniques can cause this loss, and if the amount of

loss is not quantified accurately, it could lead to false non-detections and overly aggressive upper limits. Computing signal loss correctly has subtle challenges but is necessary to ensure the accuracy of any result.

- **Error Estimation** (Section 2.2): Confidence intervals on a 21 cm power spectrum result determine the difference between a detection and a null result, which have two very different implications. Errors can be estimated in a variety of ways, and we will discuss a few of them.
- **Bias** (Section 2.3): There are several possible sources of power offset in a visibility measurement that can show up as a detection in a power spectrum, such as bias from noise and foregrounds. In particular, a successful EoR detection would also imitate a bias. Proving a bias is an EoR detection may be the most difficult challenge for 21 cm analyses, as it is crucial to be able to distinguish a detection of foreground leakage, for example, from that of EoR. In this paper we will highlight some sources of bias, discuss ways to mitigate their effects, and describe tests that a true EoR detection must pass.

#### Power Spectrum Techniques

The following techniques each have advantages when it comes to maximizing sensitivity and understanding systematics in data. However, some have limitations, and we will discuss circumstances in which there are trade-offs. We choose to focus on these four techniques because they represent major steps in PAPER’s power spectrum pipeline, with several of them also being standard steps in general 21 cm analyses.

- **Fringe-rate filtering:** Fringe-rate filtering is an averaging scheme for time-ordered data (Parsons et al. 2016). Broadly, a fringe-rate filter increases the sensitivity of a dataset and reduces the number of independent samples by an amount dependent on the width of the averaging window. However, it can also affect the presence of foregrounds and systematics. We explain the trade-offs of filtering in more detail in Section 2.1.2.
- **Weighting:** A dataset can be weighted to emphasize certain features and minimize others. One particular flavor of weighting employed by PAPER is inverse covariance weighting in frequency, which is a generalized version of inverse variance weighting that also takes into account frequency correlations (Liu & Tegmark 2011; Dillon et al. 2013; Liu et al. 2014a; Liu et al. 2014b; Dillon et al. 2014; Dillon et al. 2015). This weighting has the effect of down-weighting correlated information (i.e. foregrounds) and up-weighting noise-like information

(i.e. EoR). However, a challenge of inverse covariance weighting is in accurately defining a covariance matrix that best describes the data. We investigate the impact of different types of weighting on signal loss in Section 2.1.

- **Bootstrapping:** In addition to using theoretical models for covariance matrices and theoretical error estimation methods, bootstrapping is one way to estimate errors. Bootstrapping is a useful method for estimating errors of a dataset from itself (Andrae 2010). By randomly drawing many subsamples of the data, we obtain a sense of its inherent variance, though there are subtleties to consider such as the independence of values in a dataset. We explore this potential pitfall of bootstrapping in Section 2.2.
- **Jackknife testing:** A resampling technique useful for estimating bias, jackknives can be taken along different dimensions of a dataset to cross-validate results. In particular, null tests can be used to verify whether results are free of systematics, as done with CO power spectra (Keating et al. 2016) and CMB measurements (see e.g. Ade et al. 2008; Chiang et al. 2010; QUIET et al. 2011; Das et al. 2011; QUIET et al. 2012; Crites et al. 2015; Keck Collaboration et al. 2016; Ade et al. 2017; Sherwin et al. 2017). An EoR detection must pass jackknife and null tests, which we highlight in Section 2.3.2.

In the next three subsections, we study each theme in depth, focusing on how power spectrum technique trade-offs affect each. We use a toy data model to develop intuition into why certain analysis choices may be appealing and discuss ways in which they are limited. We highlight problems that can arise regarding each theme and offer suggestions to mitigate the issues. Ultimately, we show that rigorous investigations into signal loss, error estimation, and bias must be performed for robust 21 cm results.

#### 2.1. Signal Loss

Signal loss can arise in a variety of ways in the analysis pipeline, such as fitting a polynomial during spectral calibration, applying a delay-domain filter, or by deriving weights from data and applying them to itself. Here we focus on signal loss associated with applying a weighting matrix to data, a loss that can be significant depending on the choice of weighting and one that was previously underestimated in the A15 analysis.

Driven by the need to mitigate foreground bias, PAPER’s previous analyses use a weighting method that aims to down-weight foregrounds. This weighting is applied to data, which is then propagated into a final estimator using the power spectrum estimation technique of optimal quadratic estimators (OQE) as done in Liu & Tegmark (2011), Dillon et al. (2013), Liu et al.

(2014a), Liu et al. (2014b), Trott et al. (2012), Dillon et al. (2014), Dillon et al. (2015), and Trott et al. (2016). Before showing how signal loss can arise when using different weighting matrices, we first summarize OQE as performed in the PAPER analysis.

We begin with our data vector,  $\mathbf{x}$ , which contains our measured visibilities for a single baseline in Jy. It has length  $N_t \times N_f$ , but in practice we manipulate it as an array with dimensions  $(N_t, N_f)$ , where  $N_t$  is the number of time integrations and  $N_f$  is the number of frequency channels. Visibilities are measurements of the Fourier transform of the sky along 2 spatial dimensions (using the flat-sky approximation), and since we are interested in 3-dimensional Fourier-modes we only need to take one Fourier transform of our visibilities along the line-of-sight dimension. We do this when forming the unnormalized power spectrum estimate  $\hat{q}_\alpha$ :

$$\hat{q}_\alpha = \frac{1}{2} \mathbf{x}^\dagger \mathbf{R} \mathbf{Q}^\alpha \mathbf{R} \mathbf{x}. \quad (1)$$

Here,  $\mathbf{Q}$  is a family of matrices that takes our frequency-domain visibilities and Fourier-transforms them into power spectrum space, while also converting from Jy to Kelvin and taking into account cosmological scalings. It is evaluated as  $\mathbf{Q}^\alpha \equiv \frac{\delta \mathbf{C}}{\delta p_\alpha}$ , or the derivative of the covariance with respect to the true bandpower in  $\alpha$ , where  $\alpha$  denotes a waveband in  $k_\parallel$  ( $k_\parallel$ , a cosmological wavenumber, is the Fourier-dual to frequency under the delay approximation (Parsons et al. 2012b)).  $\mathbf{R}$  is a weighting matrix — as an example, inverse covariance weighting would set  $\mathbf{R} = \mathbf{C}^{-1}$  and an unweighted case would use  $\mathbf{R} = \mathbf{I}$ , the identity matrix.

We normalize our power spectrum estimates using the matrix  $\mathbf{M}$ :

$$\hat{\mathbf{p}} = \mathbf{M} \hat{\mathbf{q}}, \quad (2)$$

where  $\hat{\mathbf{p}}$  is the estimate of the true power spectrum. The data analyst has a choice for  $\mathbf{M}$  (subject to the constraint that window functions are sensible) — for simplicity in this section we choose  $\mathbf{M}$  to be diagonal, although we explore other cases for the analysis of PAPER-64 data as explained in Section 3.3.

In the next three sections, we investigate the effects of weighting matrices on signal loss by experimenting with different matrices  $\mathbf{R}$  and examine their impact on the resulting power spectra estimate  $\hat{\mathbf{p}}$ . Our goal in experimenting with weighting is to suppress foregrounds and investigate EoR losses associated with it. We note that we purposely take a thorough and pedagogical approach to describing the toy model examples given in the next few sections. The specifics of how signal loss appears in PAPER’s analysis is later described in Section 3.1.

### 2.1.1. Toy Model: Inverse Covariance Weighting

To build our intuition into how a particular choice of weighting, namely inverse covariance weighting, can lead to signal loss, we use a toy model. We construct a

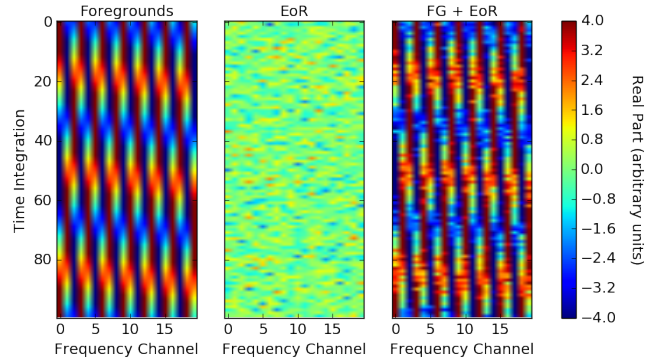


**Figure 1.** Our toy model dataset. We model a mock foreground-only visibility with a sinusoid signal that varies smoothly in time and frequency. We model a mock EoR signal as a random Gaussian signal. Real parts are shown here.

simple dataset that contains 2-dimensional data (representing visibility data with 100 time integrations and 20 frequency channels). This model represents realistic dimensions of about an hour of PAPER data which might be used for a power spectrum analysis. For PAPER-64 (both the previous analysis and our new analysis) we use  $\sim 8$  hours of data for our analysis (with channel widths of 0.5 MHz and integration times of 43 seconds), but here we scale it down for this toy model with no loss of generality.

We create mock visibilities,  $\mathbf{x}$ , and assume a non-tracking, drift scan observation. Hence, flat spectrum sources (away from zenith) oscillate in time and frequency in our measurements. We therefore form a mock bright foreground signal,  $\mathbf{x}_{FG}$ , as a complex sinusoid that varies smoothly in time and frequency, a simplistic but realistic representation of a single bright source. We also create a mock EoR signal,  $\mathbf{x}_{EoR}$ , as a complex, Gaussian random signal. A more realistic EoR signal would have a sloped power spectrum in  $\mathbf{p}(k)$  (instead of flat, as in the case of white noise), which could be simulated by introducing frequency correlations into the mock EoR signal. However, here we treat all  $k$ ’s separately, so a simplistic white noise approximation can be used. Our combined data matrix is then  $\mathbf{x} = \mathbf{x}_{FG} + \mathbf{x}_{EoR}$ , to which we apply different weighting schemes. The three data components are shown in Figure 1.

One choice for the weighting matrix  $\mathbf{R}$  is an inverse covariance matrix. This type of weighting is attractive for power spectrum analyses because it yields the smallest possible error bars on a measurement. Said differently, it gives the minimum variance estimate of the power spectrum of a signal (Tegmark 1997; Bond et al. 1998). In Liu & Tegmark (2011), it was shown that inverse covariance weighting also serves as a way to down-weight foregrounds since foregrounds have large covariances in frequency, motivating our use of the weighting for the PAPER analysis.

The covariance matrix  $\mathbf{C}$ , which describes covariances between frequency channels, can be estimated in a va-



riety of ways. Given perfect foreground, instrumental, and EoR models, we could form  $\mathbf{C}$  in a way that accurately describes our measured data. However, if our foreground model is flawed, for example, our estimate of  $\mathbf{C}$  would not be successful at down-weighting them in the data.

Therefore, one attractive way to estimate  $\mathbf{C}$  is to empirically derive it from the data  $\mathbf{x}$  itself. For instance, one could time-average such that:

$$\hat{\mathbf{C}} \equiv \langle \mathbf{x}\mathbf{x}^\dagger \rangle_t, \quad (3)$$

assuming  $\langle \mathbf{x} \rangle_t = 0$  (a reasonable assumption since fringes average to 0 over a sufficient amount of time), where  $\langle \rangle_t$  denotes a finite average over time. The weighting matrix is therefore  $\mathbf{R} = \hat{\mathbf{C}}^{-1}$ .

First, we compute the power spectrum of  $\mathbf{x}$  using OQE formalism and a weighting matrix of  $\hat{\mathbf{C}}^{-1}$ . The result is shown in green in the left plot of Figure 2. Also plotted in the figure are the unweighted ( $\mathbf{R} = \mathbf{I}$ ) power spectrum of  $\mathbf{x}_{FG}$  (blue) and  $\mathbf{x}_{EoR}$  (red).

As shown, our inverse covariance-weighted result successfully suppresses foregrounds. It is also evident that our result fails to recover the EoR signal — it exhibits the correct shape, but the amplitude level is slightly low. This is evidence of signal loss. In order to understand the behavior of this result, we can closely study our covariance eigenspectrum, shown in Figure 3.

If  $\mathbf{C}$  is computed from the data itself, it carries the risk of over-fitting information in the data and introducing a multiplicative bias (per  $k$ ) to estimates of the signal. For a mathematical derivation of signal loss arising from a data-estimated covariance matrix, see Appendix A. Here we will describe the origin of this signal loss intuitively.

If the covariance is estimated from our data, its eigenspectrum differs from the eigenspectrum of the true covariance  $\mathbf{C}$ , and this difference has consequences on our result. An eigenspectrum ranks the eigenvalues of a matrix from highest to lowest and can be thought of as a spectrum of weights that are given to each spectral mode in the data. In other words, the eigenvalues encode the strength of different shapes in the dataset. The eigenspectrum of the identity matrix  $\mathbf{I}$  is flat (all 1's) because it gives equal weighting to all modes. This is usually not the case for a covariance matrix, for which a sloped eigenspectrum means that modes are given different weights in OQE power spectrum estimation. The modes with the highest eigenvalues are down-weighted the most.

If the true covariance matrix  $\mathbf{C}$  of our data was known, then every single eigenvalue and eigenvector of  $\mathbf{C}$  would be representative of real fluctuations in the data. However, when using an estimated  $\hat{\mathbf{C}}$  that is derived from one particular data realization, its eigenvalues and eigenvectors may differ from the truth. Said differently, shapes that may not exist (or exist rarely) in a true covariance may appear stronger in the estimated covariance. Hence, they will be down-weighted more than they

should be.

In general, the strongest modes of  $\hat{\mathbf{C}}$  (highest eigenvalues) are expected to be dominated by bright foregrounds — the most prominent shapes in the data. For these ‘strong’ modes, where foregrounds outshine the EoR signal,  $\hat{\mathbf{C}} \sim \mathbf{C}$  and down-weighting these modes is beneficial. This is demonstrated in the toy model by the successful suppression of the foreground mode, where our estimated covariance matrix identifies the sinusoid shape and assigns it the highest eigenvalue (the first peak in Figure 3). In Figure 4 we show the covariances of our toy model datasets along with inverse covariance weighted data. The foreground sinusoid is clearly visible in  $\hat{\mathbf{C}}_{FG}$  but effectively absent from  $\hat{\mathbf{C}}_{FG}^{-1}\mathbf{x}_{FG}$ .

The danger of an empirically estimated covariance matrix comes from not being able to describe the ‘weak’ eigenmodes of  $\mathbf{C}$  accurately, for which the EoR signal is brighter than foregrounds. In such a case, the empirical covariance believes these modes should be down-weighted more than the true covariance would. For these modes, the error that results from not computing  $\mathbf{C}$  accurately (due to a finite data sample), has a larger impact on the ‘weak’ modes than the ‘strong’ modes. In other words, mis-estimating  $\mathbf{C}$  affects EoR-dominated eigenmodes more than FG-dominated modes, and it is primarily the error associated in down-weighting these ‘weak’ modes that leads to signal loss.

Using what we’ve learned about the eigenspectrum, we can tweak it in a simple way to suppress foregrounds and yield minimal signal loss. Recall that our toy model foreground is a sinusoid, so it can be perfectly described by a single eigenmode. Using the full dataset’s (foreground plus EoR signal) empirical covariance, we can project out the first eigenmode (i.e. use the true eigenvalue of the first eigenmode, but flatten the rest of the spectrum to have eigenvalues of 1), thereby down-weighting the foreground-dominated mode more than the rest of the modes. Hence, we are not using the relative weighting information from all the weaker eigenmodes which have comparatively larger errors. Altering  $\hat{\mathbf{C}}$  as such is one example of a regularization method, in which we are changing  $\hat{\mathbf{C}}$  in a way that flattens its eigenspectrum, making it more similar to that of  $\mathbf{I}$ . The resulting power spectrum estimate for this case is shown in the right plot of Figure 2. In this case we recover EoR, demonstrating that if we can disentangle the foreground-dominating modes from EoR-dominating modes, we can down-weight them without signal loss. There are several other ways to regularize  $\hat{\mathbf{C}}$ , and we will discuss some in Section 2.1.3.

### 2.1.2. Toy Model: Fringe-Rate Filtering

We have shown how signal loss can arise due to inaccurately characterizing weak eigenmodes (EoR dominated modes) with a data-estimated covariance. We will next show how this effect is exaggerated by reducing the total number of independent samples in a dataset.

A fringe-rate filter is an analysis technique designed



**Figure 2.** Resulting power spectrum estimates for the toy model simulation described in Section 2.1.1 — foregrounds only (blue), EoR only (red), and the weighted FG + EoR dataset (green). The power spectrum of foregrounds peaks at a  $k$  mode based on the frequency of the sinusoid used to create the mock FG signal. In the two panels, we compare inverse covariance weighting where  $\hat{\mathbf{C}}$  is derived from the data (left), and projecting out the first eigenmode only (right). In the former case, signal loss arises from using information from all eigenmodes of  $\hat{\mathbf{C}}$ . Because  $\hat{\mathbf{C}}$  is empirically estimated, its eigenvalues differ from those of the true covariance and this error primarily affects the weaker (EoR-dominated) eigenmodes. There is negligible signal loss when assigning identical weights to all eigenmodes except the first, since we are not using the relative weights of the weaker eigenmodes which  $\hat{\mathbf{C}}$  does not describe accurately.



**Figure 3.** Eigenspectrum of  $\hat{\mathbf{C}}_{FG}$  (blue),  $\hat{\mathbf{C}}_{EoR}$  (red), and  $\hat{\mathbf{C}}_{FG+EoR}$  (green). The eigenspectrum of  $\hat{\mathbf{C}}_{FG}$  peaks at the zeroth eigenmode, due to the presence of only one sinusoid. These empirically estimated covariance matrices have eigenspectra that are different from that of a true  $\mathbf{C}$ , meaning that some eigenmodes (shapes in the data) may be down-weighted more significantly than they should be, producing signal loss. Specifically, down-weighting the weak eigenmodes, where the EoR signal is greater than the FG signal, leads to loss.

to maximize sensitivity by integrating in time (Parsons et al. 2016). Rather than a traditional box-car average, a time domain filter can be designed to up-weight temporal modes consistent with the sidereal motion on the sky, while down-weighting modes which are noise-like.

Because fringe-rate filtering is analogous to averaging in time, it comes at the cost of reducing the total number of independent samples in the data. To mimic this filter, we average every four time integrations of our toy model dataset together, yielding 25 independent samples in time (Figure 5). We choose these numbers so that the total number of independent samples is similar

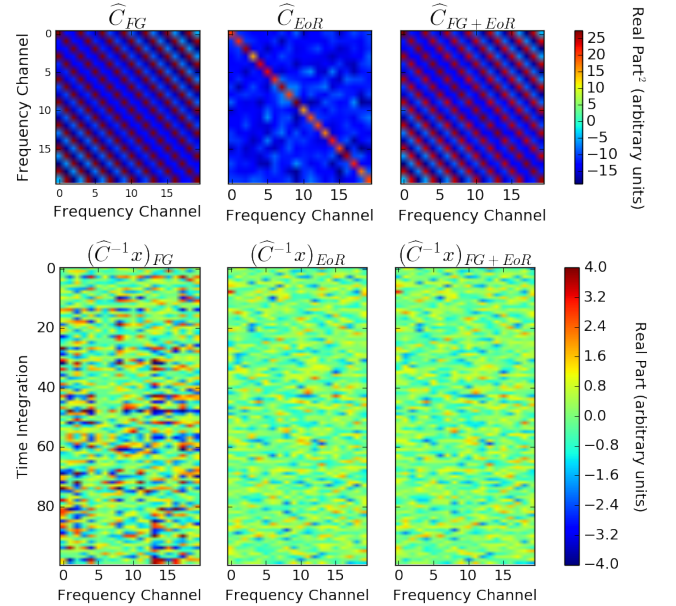


**Figure 4.** The covariance matrices (top row) and inverse covariance-weighted data (bottom row) for FG only (left), EoR only (middle), and FG + EoR (right). Real parts are shown here.

to the number of frequency channels — our matrices will still be full rank.

The resulting eigenspectrum as compared to the green curve (FG + EoR) in Figure 3 is shown in Figure 6. The spectrum, in the case of fringe-rate filtering (dashed line), falls more steeply, especially for the last few eigenmodes. In many applications, this steep fall is not indicative of the true covariance structure of the data.

With fringe-rate filtering resulting in fewer independent modes, it becomes more difficult for the empirical

covariance to estimate the true covariance matrix. This can be quantified by evaluating a convergence metric  $\varepsilon(\hat{\mathbf{C}})$  for the empirical covariance, which we define as

$$\varepsilon(\hat{\mathbf{C}}) \equiv \sqrt{\frac{\sum_{ij} (\hat{C}_{ij} - C_{ij})^2}{\sum_{ij} C_{ij}^2}}, \quad (4)$$

where  $\mathbf{C}$  is true covariance matrix. In Figure 7 we show this convergence statistic as a function of the number of independent ensemble realizations in one’s simulations (horizontal axis) and the number of independent samples in the data following fringe-rate filtering (different curve colors). With more independent time samples in the data, one converges to the true covariance more quickly.

The situation here with using a finite number of time samples to estimate our covariance is analogous to a problem faced in galaxy surveys, where the non-linear covariance of the matter power spectrum is estimated using a large — but finite — number of expensive simulations. There, the limited number of independent simulations results in inaccuracies in estimated covariance matrices (Dodelson & Schneider 2013; Taylor & Joachimi 2014), which in turn result in biases in the final parameter constraints (Hartlap et al. 2007). In our case, the empirically estimated covariances are used for estimating the power spectrum, and as we argue in Section 3.1.1 and Appendix A, the resulting estimates are biased *low*—which is precisely signal loss. In future work, it will be fruitful to investigate whether advanced techniques from the galaxy survey literature for estimating accurate covariance matrices can be successfully adapted for 21 cm cosmology. These techniques include the imposition of sparsity priors (Padmanabhan et al. 2016), the fitting of theoretically motivated parametric forms (Pearson & Samushia 2016), covariance tapering (Paz & Sánchez 2015), marginalization over the true covariance (Sellentin & Heavens 2016), and shrinkage methods (Pope & Szapudi 2008; Joachimi 2017).

Just as important as the eigenvalues are the eigenvectors of our empirical covariances. In general, different eigenvectors converge to their true forms at different rates. This is illustrated by Figure 8, which shows the convergence of eigenvectors in an empirical estimate of a covariance matrix whose true form is a diagonal matrix with eigenvalues spanning four orders of magnitude. We use as a convergence metric  $\varepsilon(\hat{\mathbf{v}})$  for the empirical eigenvectors  $\hat{\mathbf{v}}$ , defined as:

$$\varepsilon(\hat{\mathbf{v}}) \equiv \sqrt{\sum_i^{N_f} |\mathbf{v} - \hat{\mathbf{v}}|_i^2}, \quad (5)$$

where  $N_f$  is the number of frequencies (20) in the mock data. The eigenmode convergence curves in Figure 8 are ranked ordered by eigenvalue, such that “Eigenmode #0” illustrates the convergence of the eigenvector with the largest eigenvalue, “Eigenmode #1” for the second largest eigenvalue, and so on. One sees that the stronger

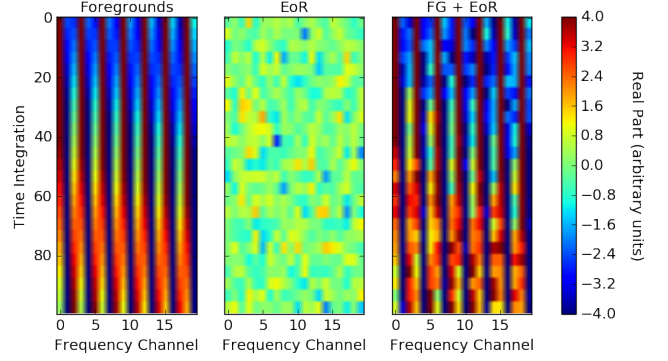


**Figure 5.** Our ‘fringe-rate filtered’ (time-averaged) toy model dataset. We average every four samples together, yielding 25 independent samples in time. Real parts are shown here.

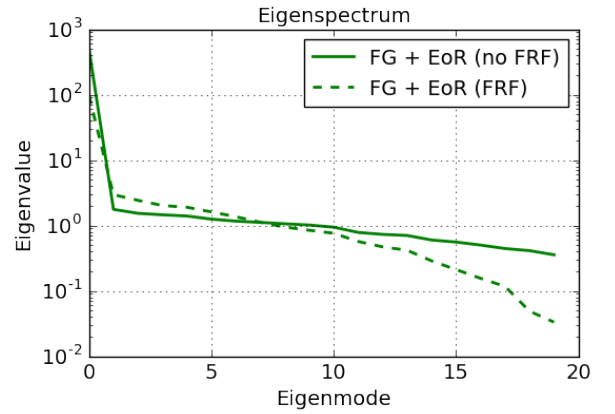


**Figure 6.** Eigenspectrum of  $\hat{\mathbf{C}}_{FG+EoR}$ , in the case of no fringe-rate filtering (solid green) and with fringe-rate filtering (dashed green).

eigenmodes converge to their true eigenvectors more quickly. With only a small number of realizations, these empirically estimated modes already retain little correlation with the specific realizations of data that were used to form the empirical covariance. As we will see in the next section, using only the strongest eigenmodes, which are less coupled to data realizations, minimizes signal loss. In contrast, the weaker eigenmodes retain more memory of the data realizations, which leads to correlations that induce signal loss.

The power spectrum results for the fringe-rate filtered toy model data is shown in Figure 9. As expected, there is a much larger amount of signal loss for this time-averaged dataset. We do a worse job estimating the true covariance and, as a result, it is a noisier estimate. This is evident by noticing that the green curve in Figure 9 fails to trace the shape of the unweighted EoR power spectrum.

Using our toy model, we have seen that a sensitivity-driven analysis technique like fringe-rate filtering has trade-offs of signal loss and noisier estimates when using data-estimated covariance matrices. Longer integrations increase sensitivity but reduce the number of indepen-

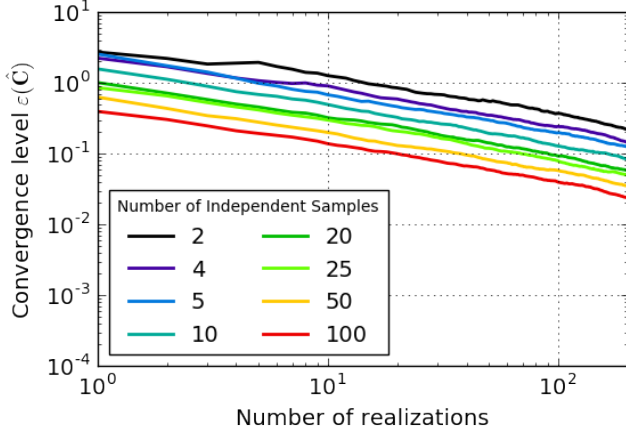


**Figure 7.** The convergence level, as defined in Equation (4), of empirically estimated covariances of mock EoR signals with different numbers of independent samples. In red, the mock EoR signal is comprised entirely of independent samples. Subsequent colors show time-averaged signals. As the number of realizations increases, we see that the empirical covariances approach the true covariances. With more independent samples, the quicker an empirical covariance converges.

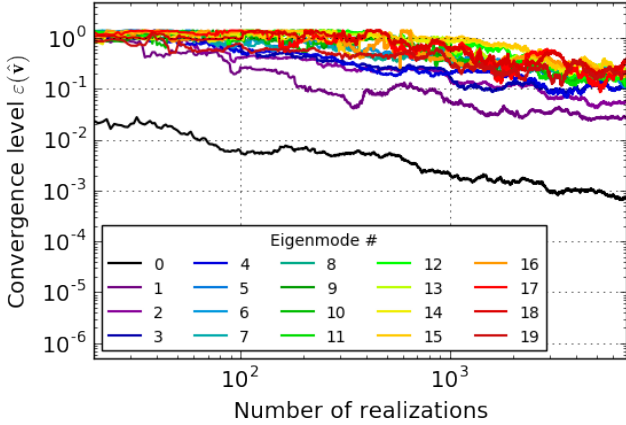


**Figure 8.** The convergence level, as defined in Equation (5), of empirically estimated eigenvectors for different number of mock data realizations. The colors span from the 0th eigenmode (the first one) to the 19th eigenmode (the last one), where they are ordered by eigenvalue in descending order. This figure shows that ‘strong’ eigenmodes (those with the highest eigenvalues) converge more quickly than ‘weak’ eigenmodes.

dent samples, resulting in poorly characterized, steep eigenspectra that can overfit signal greatly. We note that a fringe-rate filter does have a range of benefits, many described in Parsons et al. (2016), so it can still be advantageous to use one despite the trade-offs.

### 2.1.3. Toy Model: Other Weighting Options

In Section 2.1.1 we showed one example (projecting the zeroth eigenmode) of how altering  $\hat{\mathbf{C}}$  can make the difference between nearly zero and some signal loss. We will now use our toy model to describe several other ways to tailor  $\hat{\mathbf{C}}$  in order to minimize signal loss. We choose

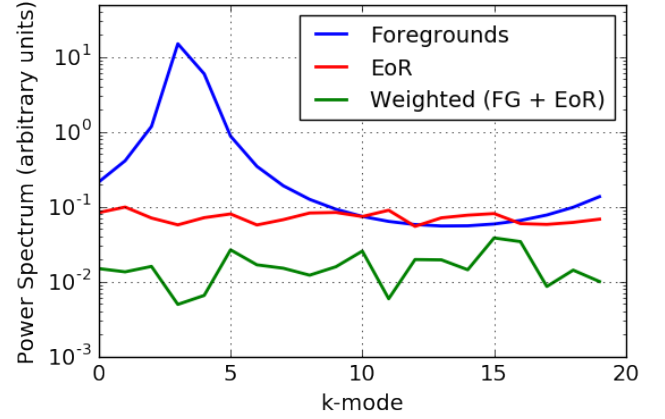


**Figure 9.** Resulting power spectrum estimate for the ‘fringe-rate filtered’ (time-averaged) toy model simulation — foregrounds only (blue), EoR only (red), and the weighted FG + EoR dataset (green). We use inverse covariance weighting where  $\hat{\mathbf{C}}$  is computed from the data. There is a larger amount of signal loss than for the non-averaged data, a consequence of a steepened, weakly characterized eigenspectrum from fewer independent modes in the data. The power spectrum estimate is also noisier, since most of the information used in constructing the estimate came from only a few eigenmodes (the weakest, EoR-dominated modes).

four independent regularization methods to highlight in this section, which have been chosen due to their simplicity in implementation and straightforward interpretations. We illustrate the resulting power spectra and eigenspectra for the different cases in Figures 10 and 11. These examples are not meant to be taken as suggested analyses methods but rather as illustrative cases.

As a first test, we model the covariance matrix of EoR as a proof of concept that if perfect models are known, signal loss can be avoided. We know that our simulated EoR signal should have a covariance matrix that mimics the identity matrix, with its variance encoded along the diagonal. We model  $\mathbf{C}_{\text{EoR}}$  as such (i.e. the identity), instead of computing it based on  $\mathbf{x}_{\text{EoR}}$  itself. Next, we add  $\mathbf{C}_{\text{EoR}} + \hat{\mathbf{C}}_{\text{FG}}$  (where  $\hat{\mathbf{C}}_{\text{FG}} = \langle \mathbf{x}_{\text{FG}} \mathbf{x}_{\text{FG}}^\dagger \rangle_t$ ) to obtain a final  $\hat{\mathbf{C}}$  to use in weighting. In Figure 10 (upper left), we see that there is negligible signal loss. This is because by modeling  $\mathbf{C}_{\text{EoR}}$ , we avoid over-fitting EoR fluctuations in the data that our model doesn’t know about (but an empirically derived  $\hat{\mathbf{C}}$  would). This is also shown by comparing the (steeper) green and (flatter) red curves in Figure 11. We don’t see perfect EoR recovery though, as the green and red curves vary slightly in Figure 10. This deviation is a consequence of the difference between the true and modeled covariance matrices. In practice such a weighting option is not feasible, as it is difficult to model  $\mathbf{C}_{\text{EoR}}$ , and  $\mathbf{C}_{\text{FG}}$  is unknown.

The second panel (top right) in Figure 10 uses a regularization method of setting  $\hat{\mathbf{C}} = \hat{\mathbf{C}} + \gamma \mathbf{I}$ , where  $\gamma = 5$  (an arbitrary strength of  $\mathbf{I}$  for the purpose of this toy model). By adding the identity matrix, element-wise, we are weighting the diagonal elements of the covariance matrix more heavily than those off-diagonal, thereby





**Figure 10.** Resulting power spectra estimates for our ‘fringe-rate filtered’ (time-averaged) toy model simulation — foregrounds only (blue), EoR only (red), and the weighted FG + EoR dataset (green). We show four alternate weighting options that each minimize signal loss, including modeling the covariance matrix of EoR (upper left), regularizing  $\hat{\mathbf{C}}$  by adding an identity matrix to it (upper right), using only the first three eigenmodes of  $\hat{\mathbf{C}}$  (lower left), and keeping only the diagonal elements of  $\hat{\mathbf{C}}$  (lower right). The first case (upper left) is not feasible in practice since we do not know  $\mathbf{C}_{FG}$  and  $\mathbf{C}_{EoR}$  like we do in the toy model.

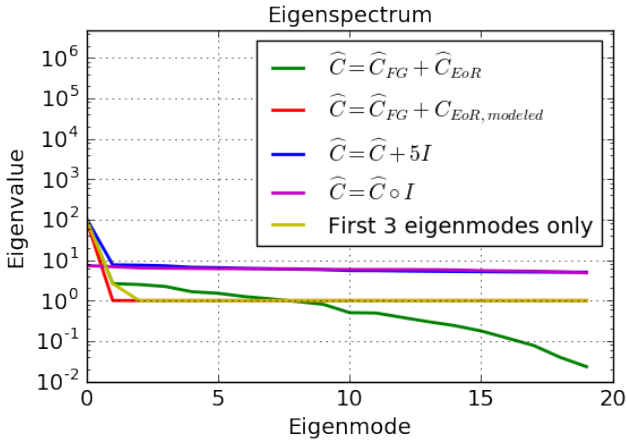


**Figure 11.** We compare the eigenspectrum of an empirically calculated  $\hat{\mathbf{C}}$  (green) to that of four alternate weighting options, including modeling the covariance matrix of EoR (red), regularizing  $\hat{\mathbf{C}}$  by adding an identity matrix to it (blue), using only the first three eigenmodes of  $\hat{\mathbf{C}}$  (yellow), and multiplying an identity matrix with  $\hat{\mathbf{C}}$  (magenta). All eigenspectra (except the green) are relatively flat and don’t exhibit signal loss. All were computed for the ‘fringe-rate filtered’ (time-averaged) toy model case presented in Section 2.1.2.

flattening out its eigenspectrum. If all modes are given similar weights, we avoid down-weighting EoR modes more than others. Although there is negligible signal loss, the small green peak at  $k \sim 3$  represents residual foregrounds that still exist since the shapes encoded in the off-diagonal frequency correlations of the covariance matrix were deemed not as prominent as the diagonal elements using this weighting scheme.

The third panel (bottom left) in Figure 10 flattens out the eigenspectrum of  $\hat{\mathbf{C}}$  a different way - by only using the first three eigenmodes. Recalling that our toy model foregrounds can be described entirely by the first eigenmode, this method intentionally projects out modes that are EoR-dominated by replacing all but the three highest weights in the eigenspectrum with 1’s (equal weights). Again, flattening the eigenspectrum results in negligible signal loss. However, we do not perfectly recover the shape of EoR because we lost information when projecting out certain modes. While this case is illuminating for the toy model, in practice it is not obvious which eigenmodes are FG vs. EoR dominated, so selecting a subset of modes to down-weight is not trivial.

The last regularization scheme we are highlighting here is setting  $\hat{\mathbf{C}} = \hat{\mathbf{C}} \circ \mathbf{I}$  (element-wise multiplication),

or inverse variance weighting (keeping only the diagonal elements of  $\hat{\mathbf{C}}$ ). In the bottom right panel of Figure 10, we see that this method does not down-weight the foregrounds. For this toy model, our foregrounds are spread out in frequency and therefore have non-negligible frequency-frequency correlations. Multiplying by the identity, element-wise, results in a diagonal matrix, meaning we are only left with correlation information between the same two frequencies. Because we disregard information from all other frequency combinations in this case, we do a poor job suppressing the foreground. But because we flattened the eigenspectrum, we also avoid signal loss. Although this method did not successfully recover EoR for this particular simulation, it is important that we show that there are many options for estimating a covariance matrix, and some may be more effective than others based on the spectral nature of the components in a dataset.

In summary, we have a choice of how to weight 21 cm data. Ideally, we want to down-weight bright foregrounds without removing the underlying cosmological signal. However, there are trade-offs between the weighting method used, its foreground-removal effectiveness, the number of independent samples in a dataset, and the amount of resulting signal loss.

## 2.2. Error Estimation

Our second major 21 cm power spectrum theme is error estimation, as we desire robust methods for determining accurate confidence intervals for our measurements. Two popular ways of calculating errors on a power spectrum measurement are calculating the variance of a dataset, and computing a theoretical error estimate based on an instrument’s system temperature and observational parameters. In a perfect world, both methods would match up. However, in practice the two don’t always agree due to a number of factors, including time, frequency, and antenna-dependent noise and non-uniform weightings.

For PAPER’s analysis, we choose to compute error bars on our measurements that have been derived from its inherent variance. A common technique used to do this is bootstrapping. For pedagogical purposes, we first define the technique of bootstrapping and then illustrate one of its pitfalls through a toy model.

Bootstrapping uses sampling with replacement to estimate a posterior distribution. For example, measurements (like power spectra) can be made from different samples of data. Each of these measurements is a different realization drawn from some underlying distribution, and realizations are correlated with each other to a degree set by the fraction of sampled points that are held in common between them. Hence, through the process of resampling and averaging along different axes, we can estimate error bars for our results which represent the underlying distribution of values that are allowed by our measurements (?: Andrae 2010).

Suppose we have  $N$  different measurements targeting

the same quantity ( $N$  power spectrum measurements). Bootstrapping means that we form  $N_{boot}$  (often a large number) bootstraps, where each bootstrap is a random selection of the  $N$  measurements. Bootstraps each have dimensions of  $N$ , and the values populated into each bootstrap are drawn from the original set of measurements with replacement (i.e. every  $N$ th slot is filled randomly for each bootstrap). Next we take the mean of each bootstrap to collapse it from an array of length  $N$  to a single number (we are interested in the mean statistic here, but any function of interest can be applied to each bootstrap as long as it’s the same function for each one). The error (on the mean) is then computed as the standard deviation across all bootstraps.

We must be careful in distinguishing  $N_{boot}$ , the number of bootstraps, from  $N$ , the number of samples, or elements, or values, that comprise a bootstrap. In the toy models presented in this section,  $N_{boot}$  is typically large, and the standard deviation across bootstraps (the error we are computing) converges for large  $N_{boot}$ . It is the value of  $N$  that we must be careful in setting, as described in the rest of this section.

For our toy model, suppose we have a Gaussian random signal dataset of length  $N = 1000$  and unity variance (zero mean). This could represent 1000 power spectrum measurements, for which we are interested in its error. We predict that the error on the mean should obey  $1/\sqrt{N}$ , where  $N$  is the number of samples.

We next form 500 bootstraps ( $N_{boot} = 500$ ). To create each bootstrap, we draw  $N$  samples, with replacement, of the original data, and take the mean over the  $N$  samples. The standard deviation over the 500 bootstraps gives an error estimate for our dataset. This error is indicated by the gray star in Figure 12 and matches our theoretical prediction (green).

One major caveat of bootstrapping arises when working with correlated data. If, for example, a dataset has many repeated values inside it, this would be reflected in each bootstrap. The same value would be present multiple times within a bootstrap and also be present between bootstraps, purely because it has a more likely chance of being drawn if there are repeats of itself. Therefore, bootstrapping correlated data results in a smaller variation between bootstraps, and hence, under-estimates errors. The use of a fringe-rate filter, which averages data in time to increase sensitivity, is one example which leads to a reduction in the number of independent samples, creating a situation in which errors can be underestimated. We will now show this effect using our toy model.

Going back to our toy model, we apply a sliding box-car average to 10 samples at a time, thus reducing the number of independent data samples to  $N/10 = 100$ . Bootstrapping this time-averaged noise, using the same method as described earlier (drawing  $N=1000$  elements per bootstrap sample), under-estimates the error by a factor of  $\sim 3$  (black points in Figure 12, at  $N=1000$ ). This occurs because we are drawing more samples than

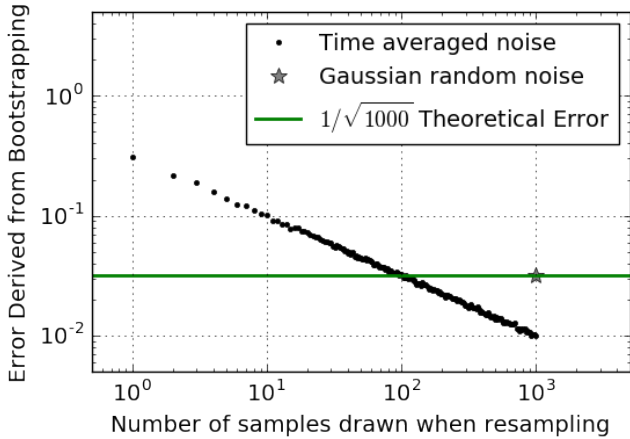


**Figure 12.** Error estimation from bootstrapping as a function of the number of elements drawn per bootstrap when sampling with replacement. The star represents the standard deviation of  $N_{boot} = 500$  bootstraps, each created by drawing 1000 elements (with replacement) from a length 1000 array of a Gaussian random signal. The black points correspond to time-averaged data (correlated data) which has 100 independent samples. They illustrate how errors can be under-estimated if drawing more elements than there are independent samples in the data. The estimated errors match up with the theoretical prediction only at  $N = 100$ .

independent ones available, and thus some samples are repeated multiple times in all bootstraps, leading to less variation between the bootstraps. In fact, the error derived from bootstrapping is a strong function of the number of elements that are drawn per bootstrap (Figure 12, black points), and we can both under-estimate the error by drawing too many or over-estimate it by drawing too few. However, since we know that we have 100 independent samples in this toy model, the error associated with drawing  $N=100$  samples with replacement does match the theoretical prediction as expected (the black points cross the green line at  $N=100$  in Figure 12).

This example highlights the importance of understanding how analysis techniques (e.g. fringe-rate filtering) can affect a common statistical procedure like bootstrapping. Bootstrapping as a means of estimating power spectrum errors from real fringe-rate filtered data requires knowledge of the number of independent samples, which is not always a trivial task. For example, computing the effective number of independent samples of fringe-rate filtered data is not as simple as counting the number of averages performed. Down-sampling a time-averaged signal is straightforward using a boxcar average, but non-trivial with a more complicated convolution function that has long tails. Hence, we do not recommend bootstrapping unless the number of independent samples along the axis that is being re-sampled is well-determined.

In summary, bootstrapping can be an effective and straightforward way to estimate errors of a dataset. However, we have illustrated a situation in which bootstrapping can lead to under-estimated errors and there-

fore under-estimated power spectrum limits. We have shown that bootstrapped error depends strongly on the number of elements drawn in a bootstrap sample. Estimated errors can drop to arbitrarily small values when the number of elements drawn exceeds the effective number of independent elements. While bootstrapping is convenient because it provides a way to estimate errors from the data itself, one must assess whether certain analysis choices have compromised the method and whether a variation or an avoidance of traditional re-sampling could be preferred instead.

### 2.3. Bias

In a 21 cm power spectrum, detections could be the EoR signal, but they could also be attributed to other sources of bias. Connecting a detection to EoR as opposed to noise or foreground bias is a key challenge of future 21 cm data analyses (e.g. Petrovic & Oh 2011). In this section we will discuss possible sources of bias in a measurement, as well as techniques that can help mitigate their effects. We will also present a series of tests in a pedagogical fashion which we suggest be used to help evaluate deep limits and/or detections.

#### 2.3.1. Foreground and Noise Bias

Foreground bias is perhaps one of the main factors limiting 21 cm results. Foreground signals lie  $\sim 4$ -5 orders of magnitude above the cosmological signal. Though there are many techniques proposed for removing foregrounds (see e.g. Vedantham et al. 2012; Parsons et al. 2012a; Parsons et al. 2012b; Dillon et al. 2013; Wang et al. 2013; Parsons et al. 2014; Liu et al. 2014a; Liu et al. 2014b; Dillon et al. 2015; Pober et al. 2016; Trott et al. 2016), most experiments currently remain limited by residuals rather than noise, especially at low  $k$ .

For a particular baseline length, there is a maximum delay imposed on sources attached to the sky, which corresponds to the light-crossing time between two antennas in a baseline. For longer baselines, this value increases, producing what is known as “the wedge” (Datta et al. 2010; Parsons et al. 2012b; Vedantham et al. 2012; Pober et al. 2013; Thyagarajan et al. 2013; Liu et al. 2014a,b; Patil et al. 2017). The wedge describes a region in  $k$ -space contaminated by smooth spectrum foregrounds, bounded by baseline length (which is proportional to  $k_{\perp}$ ) and delay (which is proportional to  $k_{\parallel}$ ). Properties of the wedge can be used to isolate and avoid foregrounds, as done by A15, Parsons et al. (2014), Dillon et al. (2014), Dillon et al. (2015), Jacobs et al. (2015), Beardsley et al. (2016), and Trott et al. (2016).

Although smooth spectrum foregrounds preferentially show up at low delay, or low  $k$  modes, their isolation within the wedge is not perfect. In deep measurements, power spectrum measurements at  $k_{\parallel}$  values beyond the length of a baseline are often still contaminated at a low level. This leakage, particularly at low  $k$ ’s, can be attributed to convolution kernels associated with Fourier-transforming visibilities into delay-space.

In other words, smooth-spectrum foregrounds appear as  $\delta$ -functions in delay-space, convolved by the Fourier transform of the source spectrum, the signal chain, and the antenna response, all of which could smear out the foregrounds and cause leakage outside the wedge (e.g. Ewall-Wice et al. 2017).

There are analysis techniques to mitigate the effects of foreground leakage and prevent information from low  $k$ 's from spreading to high  $k$  values. For example, narrow window functions in delay-space can be used to minimize the covariance of a particular  $k$  value with other ones (Liu et al. 2014b). In other words, one can construct an estimator using OQE that forces a window function to have a minimum response to low  $k$  values. The window function used in A15 is constructed in such a way, specifically to prevent foregrounds that live at low  $k$ 's from contaminating higher  $k$ -modes (see Section 3.3). Minimizing foreground leakage in this way however, comes with the trade-off of compromising power spectrum sensitivity, since narrow window functions increases errors for each  $k$ -mode (Liu et al. 2014b).

Determining the source of detections at higher  $k$ 's is more difficult. In previous power spectrum results, these detections have been explained as instrumental systematics, particularly time-variable cross talk, RFI, cable reflections, and calibration errors (A15; Parsons et al. 2014; Dillon et al. 2014; Beardsley et al. 2016; Patil et al. 2017). In the next section (Section 2.3.2), we will present some tests that can help distinguish these excesses from that of EoR.

In addition to foreground bias, noise can also be responsible for positive power spectrum detections if thermal noise is multiplied by itself. Every 21 cm visibility measurement contains thermal noise that is comprised of receiver and sky noise. We expect this noise to be independent between antennas and thus we can beat it down (increase sensitivity) by integrating longer, using more baselines, etc. However, the squaring of noise occurs when cross-multiplying visibilities, which is shown by the two copies of  $\mathbf{x}$  in Equation (1). If both copies of  $\mathbf{x}$  come from the same baseline and time, it can result in power spectrum measurements that are higher than those predicted by the thermal noise of the instrument. One way to avoid this type of noise bias is to avoid cross-multiplying data from the same baselines or days. This ensures that the two quantities that go into a measurement have separate noises that don't correlate with each other. We also note that if the noise level is known, this type of bias can be subtracted off, though this procedure is argued to be dangerous by Dillon et al. (2014).

Another type of noise bias can stem from the spurious cross-coupling of signals between antennas. This excess is known as instrumental crosstalk and is an inadvertent correlation between two independent measurements via a coupled signal path. Crosstalk appears as a constant phase bias in time in visibilities, and it varies slowly compared to the typical fringe-rates of sources. Because it

is slow-varying, crosstalk can be suppressed using time-averages or fringe-rate filters. However, there remains a possibility that power spectrum detections are caused by residual, low-level crosstalk which survived any suppression techniques.

### 2.3.2. Jackknife Tests

We now approach the difficult task of tracing excesses to foreground, noise, and EoR biases through a discussion of useful jackknife tests. Again, we first approach this topic pedagogically as an introduction to the related PAPER discussion in Section 3.3.

The jackknife is a resampling technique in which a statistic (i.e. power spectrum) is computed in subsets of the data (?; ?). These subsets are then compared to reveal systematics. In this section we define two main tests — the null test and the traditional jackknife — and explain how a power spectrum detection must pass each. We then highlight how these tests can be used to help distinguish between different sources of bias.

- **Null Test:** A null test is a type of jackknife test that removes the astronomical signal from data in order to investigate underlying systematics (e.g., see Keating et al. (2016) for examples from intensity mapping that are closely related to our current application). For example, one can divide data into two subsets by separating odd and even Julian dates, or the first half of the observing season from the second. Subtracting the two removes signal that is common to both subsets, including foregrounds and EoR. The resulting power spectrum should be consistent with thermal noise estimates; if it is not, it suggests the presence of a systematic that differs from one of the data subsets to the other (i.e. doesn't get subtracted perfectly).
- **Traditional Jackknife:** In a broader sense, it is important to perform many jackknife tests in order to instill confidence in a final result. A stable result must be steadfast throughout all jackknives no matter how the data is sliced. Jackknives can be taken along several different axes — for example, one could start with a full dataset, and compute a new power spectrum every time as a day of data is removed, or a baseline is removed. This type of jackknife would reveal bias present only at certain LSTs (such as a foreground source), for example, or misbehaving baselines.

While the null test hunts for deviations from thermal noise and the jackknife tests for deviations in subsamples, they are both closely related. We can highlight the connection between the two using a toy model dataset.

Suppose we have two measurements (for example, from two baselines),  $\mathbf{x}_a$  and  $\mathbf{x}_b$ . The measurements have dimensions of 200 time integrations and 20 frequency channels. They each have separate thermal noises constructed as a Gaussian random signal for each, and identical EoR signals.



To mimic the presence of a systematic in part of the measurement, we add a toy sinusoid foreground, similar to the one used in Section 2.1.1, to the first 100 time integrations of both measurements. This represents a foreground signal present in, for example, the first half of the LST range used for analysis, but not the second half. Mathematically, if  $\mathbf{n}$  is noise,  $\mathbf{e}$  is the EoR signal, and  $\mathbf{fg}$  is the foreground signal, the two measurements (which are cross-multiplied to form power spectra) can be written as:

$$\mathbf{x}_a = \mathbf{n}_a + \mathbf{e} + \mathbf{fg} \quad (6)$$

and

$$\mathbf{x}_b = \mathbf{n}_b + \mathbf{e} + \mathbf{fg}. \quad (7)$$

The two jackknife samples are  $\mathbf{x}_1$  and  $\mathbf{x}_2$ , representing jackknives in time. These can be written (for both measurements  $a$  and  $b$ ) as:

$$\mathbf{x}_1 = \mathbf{n} + \mathbf{e} + \mathbf{fg} \quad (8)$$

$$\mathbf{x}_2 = \mathbf{n} + \mathbf{e} \quad (9)$$

For example,  $\mathbf{x}_{1a}$  represents a jackknife sample (first half of the data) for the first measurement. Similarly,  $\mathbf{x}_{2b}$  represents a jackknife sample (second half of the data) for the second measurement.

We do not perform a time-average or apply a fringe-rate filter to this toy model, since we are interested only in what jackknife tests can tell us about biases. For the same reason, we use a weighting matrix of  $\mathbf{I}$  for power spectrum estimation to avoid signal loss.

We form three different power spectrum estimates shown in Figure 13. The first is a null test where we subtract  $\mathbf{x}_2$  from  $\mathbf{x}_1$  for both measurements  $a$  and  $b$ . This is equivalent to splitting up a full dataset along an axis (in this case, time) and subtracting the two to remove sky signal that should ideally be present in both. We cross-multiply measurements  $a$  and  $b$  to form an un-biased (thermal noise-wise) estimate (blue curve). The second estimate, shown in red, is the same null test with the foreground systematic removed (eliminate  $\mathbf{fg}$  in Equations 6 and 7). Finally, we also show the noise power spectrum (green).

From this test we see a clear difference between the null test with the presence of the foregrounds, and the power spectrum of noise. This signifies a non-EoR bias that is only present in either  $\mathbf{x}_1$  or  $\mathbf{x}_2$ , but not both.

While the null test is useful for testing noise properties and the uniformity of a dataset, jackknives are useful in pinpointing which data subsets are contaminated by biases and which are not; in our toy model we see that the bias exists only in  $\mathbf{x}_1$  (Figure 14). If foreground or noise biases exist in a dataset, jackknives can tease them out and provide insight into possible sources. For example, if jackknives along the time-axis reveal a bias present at a certain LST, a likely explanation would be excess foreground emission from a radio source in the

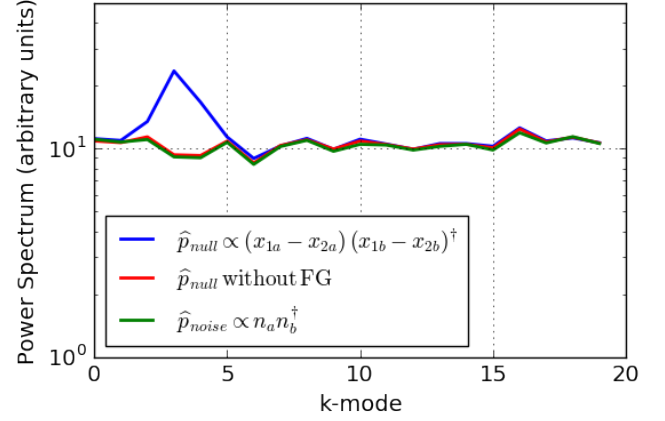


**Figure 13.** Power spectrum estimates for a null jackknife test with the presence of a foreground systematic (blue), without the foreground systematic (red), and noise alone (green). Because the first null test is not consistent with noise, it suggests the presence of a systematic in either  $\mathbf{x}_1$  or  $\mathbf{x}_2$ . Null tests of clean measurements should be consistent with thermal noise.

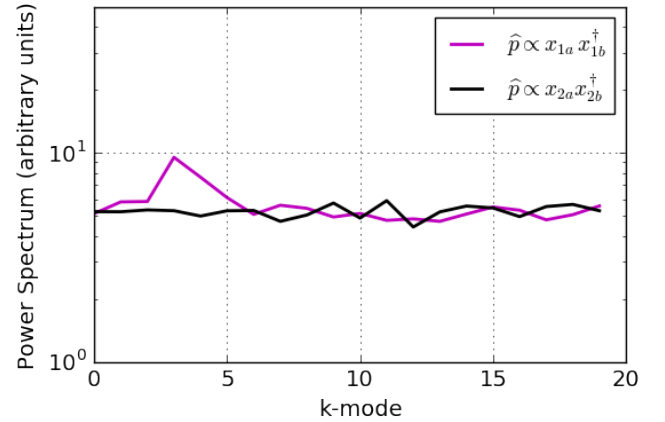


**Figure 14.** Power spectrum estimates for  $\mathbf{x}_1$  and  $\mathbf{x}_2$ , two jackknives of the toy model. They suggest the presence of a systematic in  $\mathbf{x}_1$  only (which is exactly what was put in), illustrating how jackknives can be used to tease out excesses. Clean measurements should remain consistent despite the jackknife taken.

sky at that time. A jackknife test involving data before and after the application of a fringe-rate filter can reveal whether cross-talk noise bias is successfully suppressed with the filter, or if similar-shaped detections in both power spectra suggest otherwise. There are many other jackknife axes of which we will not go into detail here, including baseline, frequency, and polarization. Ultimately, an EoR detection should persist through them all and a clean measurement should exhibit noise-like null spectra.

In this section we have highlighted how null tests and jackknife tests are key for determining the nature of a power spectrum detection. In Section 3.3 we perform some examples of these tests on PAPER-64 data in order to prove that our excesses are not EoR and to identify their likely cause.

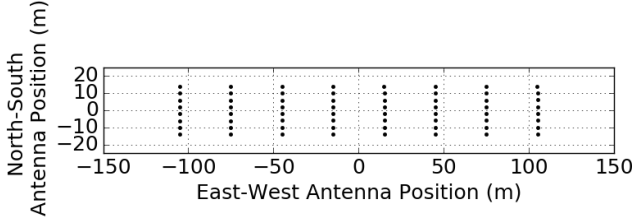


**Figure 15.** The PAPER-64 antenna layout. We use only the 30 m East/West baselines for the revised analysis in this paper (i.e. the shortest horizontal spacings).

### 3. DEMONSTRATION IN PAPER-64 DATA

In the previous sections we have discussed three overarching 21 cm power spectrum themes — signal loss, error estimation, and bias. Understanding the subtleties and trade-offs involved in each is necessary for an accurate and robust understanding of a power spectrum result.

We now present a case study of these same three themes using data from the PAPER experiment. We use the intuition developed through the toy model simulations in order to make a new analysis of the PAPER-64 dataset originally presented in A15 and obtain a revised power spectrum estimate.

As a brief review, PAPER is a dedicated 21 cm experiment located in the Karoo Desert in South Africa. The PAPER-64 configuration consists of 64 dual-polarization drift-scan elements that are arranged in a grid layout. For our case study, we focus solely on Stokes I estimated data (Moore et al. 2013) from PAPER’s 30 m East/West baselines (Figure 15). All data is compressed, calibrated (using self-calibration and redundant calibration), delay-filtered (to remove foregrounds inside the wedge), LST-binned, and fringe-rate filtered. For detailed information about the backend system of PAPER-64, its observations, and data reduction pipeline, we refer the reader to Parsons et al. (2010) and A15. We note that all data processing steps are identical to those in A15 until after the LST-binning step in Figure 3 of A15.

The previously best published 21 cm upper limit result from A15 uses 124 nights of data to place a  $2\sigma$  upper limit on  $\Delta^2(k)$ , defined as

$$\Delta^2(k) = \frac{k^3}{2\pi^2} \hat{\mathbf{p}}(\mathbf{k}), \quad (10)$$

of  $(22.4 \text{ mK})^2$  in the range  $0.15 < k < 0.5 \text{ h Mpc}^{-1}$  at  $z = 8.4$ . The revision of this limit (Kolopanis et al., *in prep*) stems from previously underestimated signal loss and underestimated error bars, both of which we address in the following sections.

For our analysis, we use 8.1 hours of LST (RA 0.5–8.6 hours) and 51 total baselines (A15 uses a slightly different RA range of 0–8.6 hours). All power spectrum results are produced for a center frequency of 151 MHz using a width of 10 MHz (20 channels), identical to the analysis in A15. We note that, besides using only one

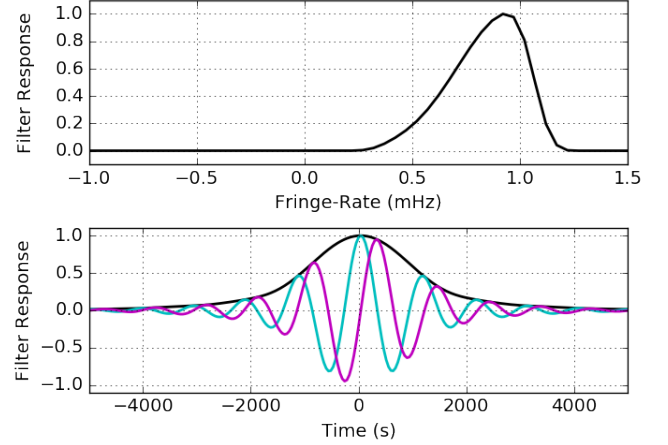


**Figure 16.** Top: the normalized optimal power-spectrum sensitivity weighting in fringe-rate space for our fiducial baseline and Stokes I polarization beam. Bottom: the time-domain convolution kernel corresponding to the top panel. Real and imaginary components are illustrated in cyan and magenta, respectively, with the absolute amplitude in black. The fringe-rate filter acts as an integration in time, increasing sensitivity but reducing the number of independent samples in the dataset.

baseline type instead of the three as in A15, the PAPER-64 dataset that we use in this case study differs from that in A15 only in the analysis. The most significant changes occur in the power spectrum analysis, which is explained in the rest of this paper, but we also note that the applied fringe-rate filter is also slightly different. In A15, the applied filter was degraded by widening it in fringe-rate space. This was chosen in order to increase the number of independent modes and reduce signal loss, though as we will explain in the next section, this signal loss was still under-estimated. With the development of a new, robust method for assessing signal loss, we choose to use the optimal filter in order to maximize sensitivity. This filter is computed for a fiducial 30 m baseline at 150 MHz, the center frequency in our band. The filter in both the fringe-rate domain and time domain is shown in Figure 16.

#### 3.1. PAPER-64: Signal Loss

In Section 2.1, we showed how signal loss arises when weighting data using information from the data itself. Here we describe a methodology for estimating the amount of signal loss caused by a particular power spectrum estimator when applied to a particular data set. There is, of course, no way of determining an exact signal loss “correction factor,” i.e., we cannot perfectly undo the effects of a lossy estimator. In this work, we inject simulated cosmological signals into our data and test the recovery of those signals in order to statistically quantify the amount of signal loss accompanying a weighting scheme used in OQE power spectrum estimation. There are, in fact, several different ways of incorporating the result of such a calculation into a revised power spectrum estimate which accounts for signal loss. In this section, we describe a methodology for de-

termining an approximate correction factor which can be applied to a power spectrum estimate; in Appendix B, we present an alternate framework that explicitly interprets all measurements as upper limits in the presence of signal loss. These two methods yield very similar results, but fundamentally are answering subtly distinct questions. We also highlight major differences from the signal loss computation used in A15, which previously underestimated losses.

### 3.1.1. Signal Loss Methodology

To capture the full statistical likelihood of signal loss, one requires a quick way to generate many realizations of simulated 21 cm signal visibilities. Here we use the same method as in A15, where mock Gaussian noise visibilities (mock EoR signals) are filtered in fringe-rate space to retain only “sky-like” time-modes. This signal is then added to the data.<sup>1</sup>

Suppose that  $\mathbf{e}$  is the injected EoR (at some amplitude level), and  $\mathbf{x}$  is our data. We define  $\mathbf{r}$  to be the data plus the EoR signal:

$$\mathbf{r} = \mathbf{x} + \mathbf{e}. \quad (11)$$

We are interested in quantifying how much variance in  $\mathbf{e}$  is lost after weighting  $\mathbf{r}$  and estimating the power spectrum according to OQE formalism. We investigate this by comparing two quantities we call the input power spectrum and output power spectrum:  $P_{\text{in}}$  and  $P_{\text{out}}$ , defined as

$$P_{\text{in},\alpha} \equiv M_{\text{in}}^\alpha \mathbf{e}^\dagger \mathbf{I} \mathbf{Q}^\alpha \mathbf{I} \mathbf{e} \quad (12)$$

and

$$\begin{aligned} P_{\text{out},\alpha} &\equiv \hat{\mathbf{p}}_{r,\alpha} - \hat{\mathbf{p}}_{x,\alpha} \\ &= M_r^\alpha \mathbf{r}^\dagger \mathbf{R}_r \mathbf{Q}^\alpha \mathbf{R}_r \mathbf{r} - M_x^\alpha \mathbf{x}^\dagger \mathbf{R}_x \mathbf{Q}^\alpha \mathbf{R}_x \mathbf{x}, \end{aligned} \quad (13)$$

where, for illustrative purposes and notational simplicity, we have written these equations with diagonal normalization matrices  $M$ , even though for our numerical results we use a full non-diagonal matrix  $\mathbf{M}$  as in Equation (2).  $P_{\text{in}}$  represents the unweighted power spectrum of  $\mathbf{e}$ , our simulated EoR signal,  $\hat{\mathbf{p}}_x$  is the power spectrum of the data alone,  $\hat{\mathbf{p}}_r$  is the power spectrum of the data plus injection, and  $P_{\text{out}}$  is the difference between  $\hat{\mathbf{p}}_r$  and  $\hat{\mathbf{p}}_x$ .

In short, we can approximate a signal loss estimate as the ratio of  $P_{\text{out}}/P_{\text{in}}$ , evaluated at the data level  $\hat{\mathbf{p}}_x$ . We motivate the fact that we can evaluate the output-to-input power spectrum ratio at  $\hat{\mathbf{p}}_x$  by the following

<sup>1</sup> One specific change from A15 is that we add this simulated signal into the analysis pipeline before the final fringe-rate filter is applied to the data. Previously, the addition was done after that final fringe-rate filter step. This change results in an increased estimate of signal loss, likely due to the use of the fringe-rate filter as a simulator. However, this pipeline difference, while significant, is not the dominant reason why signal loss was under-estimated in A15 (the dominant reason is explained in the main text).

reasoning (and then detail our signal loss estimation in practice in the sections that follow).

In the limit of no instrumental noise, the data that we measure,  $\mathbf{x}$ , is comprised of two signals, such that

$$\mathbf{x} \equiv \mathbf{f} + \mathbf{s}, \quad (14)$$

where  $\mathbf{f}$  represents the foregrounds and  $\mathbf{s}$  represents the cosmological signal. In general, suppose that our power spectrum algorithm passes the data through some function  $g$ , yielding a lossy estimate of the power spectrum  $\hat{\mathbf{p}}_x$ . This can be parametrized as

$$\langle \hat{\mathbf{p}}_x \rangle = \langle g(\mathbf{x}) \rangle = \ell_{\text{fg}} \mathbf{p}_{\text{fg}} + \ell_{\text{eor}} \mathbf{p}_{\text{eor}}, \quad (15)$$

where  $\ell_{\text{eor}}$  and  $\ell_{\text{fg}}$  are multiplicative factors accounting for the signal loss in the true EoR power spectrum  $\mathbf{p}_{\text{eor}}$  and true foreground power spectrum  $\mathbf{p}_{\text{fg}}$ , respectively. It is not *a priori* obvious why this parameterization is suitable; we thus provide a toy model in Appendix A to motivate this, although it should be noted that the result is an approximation.

Given this form, a suitable estimate for  $\mathbf{p}_{\text{eor}}$  would be  $\hat{\mathbf{p}}_x/\ell_{\text{eor}}$ , or the uncorrected power spectrum of data divided by the signal loss estimate. Although such an estimate leaves an additive bias from foregrounds that must be mitigated by other methods (as is the case for any attempt to measure the 21 cm power spectrum), it normalizes  $\mathbf{p}_{\text{eor}}$  back to its correct level such that there is no multiplicative bias. The most conceptually straightforward way to compute  $\ell_{\text{eor}}$  is to model the foregrounds and EoR signal via simulations, and then to form the quantity

$$\hat{\ell}_{\text{eor}} = \frac{g(\mathbf{f} + \mathbf{s}) - g(\mathbf{f})}{\mathbf{p}_{\text{eor}}}. \quad (16)$$

However, this approach assumes that we have sufficiently good knowledge of our foreground and signal models, which is certainly not the case — if it were, it would be simpler to construct our covariance matrices from our models, avoiding signal loss altogether! Instead, we can use the data itself as our model of the foregrounds, injecting a new EoR signal  $\mathbf{e}$  (with power spectrum  $P_{\text{in}}$ ), computing instead

$$\hat{\ell}_{\text{eor}} = \frac{g(\mathbf{x} + \mathbf{e}) - g(\mathbf{x})}{P_{\text{in}}}, \quad (17)$$

which reduces to the same result because of the linearity of Equation (15). Essentially, one is computing the slope of  $\langle \hat{\mathbf{p}}_x \rangle$  with respect to  $\mathbf{p}_{\text{eor}}$  (note that both Equations (16) and (17) take the form of finite difference derivatives). Under the approximation that the relation between the two quantities is linear, it does not matter whether this slope is evaluated about  $\mathbf{x}$  or  $\mathbf{f}$ . In reality, one expects some deviations from linearity, but Equation (17) remains a good approximation of Equation (16) as long as  $\mathbf{x}$  is dominated by  $\mathbf{f}$ .

Using this motivation, the numerator of Equation (17) is precisely our expression for  $P_{\text{out}}$  (Equation (13)), and the denominator is  $P_{\text{in}}$  (Equation (12)), where the function  $g$  is our OQE power spectrum pipeline. [DCJ:

Here is the post-hoc justification for this signal loss method. Except goes back to assumption of equation for  $g$  which just *assumes* that there are no cross terms in the estimation of a power spectrum. So we're just kicking the can down the road.] [ACL: Ok, in my defense, Equation (15) is a little better than an *assumption*. Appendix (A) does in fact illustrate this with an example. The crucial question is whether we're allowed to motivate our method based on a relationship that is only true in expectation. Note that this expectation includes allowances for signal loss due to the cross correlation between signal and foregrounds, with an example of this being Appendix A.] [JCP: I'm fine with leaving the text as is and calling this note closed with the addition of the appendix, but will wait for sign off from DCJ.] Effectively, this means that the relationship between the input and output power spectra,  $P_{\text{in}}$  and  $P_{\text{out}}$ , can be thought of as a transfer function which, for a sampling of  $P_{\text{in}}$  and  $P_{\text{out}}$  provides a mapping from an input power spectrum distribution into an output distribution. By viewing data through this signal loss lens, we may then ask the question "what input power spectrum distribution could this (signal-loss affected) data come from?"

In Section 3.1.2, we provide some intuition for how the transfer function is able to capture signal loss, and why this signal loss occurs in the first place. Section 3.1.3 then details the numerical computations used to translate our power spectrum result into one viewed through a signal loss lens. We note that interpretation of the signal injection results can be framed in multiple ways which yield similar but not identical answers. One alternative to the method described in Section 3.1.3 is described in Appendix B.

### 3.1.2. Signal Loss Illustration

To explore how our expression for  $P_{\text{out}}$  encapsulates signal loss, we expand out Equation (13):

$$\begin{aligned} P_{\text{out},\alpha} &= M_r^\alpha (\mathbf{x} + \mathbf{e})^\dagger \mathbf{R}_r \mathbf{Q}^\alpha \mathbf{R}_r (\mathbf{x} + \mathbf{e}) - M_x^\alpha \mathbf{x}^\dagger \mathbf{R}_x \mathbf{Q}^\alpha \mathbf{R}_x \mathbf{x} \\ &= M_a^\alpha \mathbf{x}^\dagger \mathbf{R}_r \mathbf{Q}^\alpha \mathbf{R}_r \mathbf{x} + M_b^\alpha \mathbf{e}^\dagger \mathbf{R}_r \mathbf{Q}^\alpha \mathbf{R}_r \mathbf{e} \\ &\quad + M_c^\alpha \mathbf{x}^\dagger \mathbf{R}_r \mathbf{Q}^\alpha \mathbf{R}_r \mathbf{e} + M_d^\alpha \mathbf{e}^\dagger \mathbf{R}_r \mathbf{Q}^\alpha \mathbf{R}_r \mathbf{x} \\ &\quad - M_x^\alpha \mathbf{x}^\dagger \mathbf{R}_x \mathbf{Q}^\alpha \mathbf{R}_x \mathbf{x}. \end{aligned} \quad (18)$$

We see that  $P_{\text{out}}$  is comprised of multiple terms. To build intuition into each of these terms, they are plotted individually in Figure 17 for two cases: inverse covariance weighting ( $\mathbf{R}_r = \hat{\mathbf{C}}_r^{-1}$ , left) and unweighted ( $\mathbf{R}_r = \mathbf{I}$ , right). We leave the details of the simulation to Section 3.1.3, but for now highlight that each term in Equation (18) corresponds to a different color in the plot. Specifically, the first term in Equation (18) is plotted as blue, the second as green, the third and fourth (which are the same) as red, and the last as gray. The solid black curve denotes  $P_{\text{out}}$ , which is comprised of all the other terms.

A brief description of Figure 17 is as follows. The gray curve represents the data level, which is constant as the level of  $P_{\text{in}}$ , the input EoR signal, is changed. The blue curve is the power spectrum of the data only, weighted by an empirical covariance estimated from the data plus the EoR signal ( $\hat{\mathbf{C}}_r^{-1}$ ). It approaches the gray at low injection level, as expected, since in that case  $\hat{\mathbf{C}}_r^{-1} \rightarrow \hat{\mathbf{C}}_x^{-1}$ . The green curve is the power spectrum of the EoR signal, weighted by  $\hat{\mathbf{C}}_r^{-1}$ . This is the exact term that was compared to  $P_{\text{in}}$  in the A15 signal loss analysis, and in doing so this would imply there is negligible loss (where the green crosses the gray). It is primarily due to the cross-terms (red), that the black curve exhibits  $\sim 3$  orders of magnitude of loss at the data level, for the inverse covariance weighted case. We see that the cross-terms can produce a large, negative signal which serves to reduce  $P_{\text{out}}$  and drive the bulk of our loss. In the unweighted case, however (right plot), the cross-terms primarily drive a tail of 'excess'  $P_{\text{out}}$  at low injects, though at larger injects we see unity transfer as expected (the solid black curve lies on the dotted black line, which represents unity transfer).

We now turn to building intuition behind the negative power that arises from the cross-terms in Equation (18). For illustrative purposes in this subsection only, we consider a scenario where  $\mathbf{e}$  dominates compared to  $\mathbf{x}$ . It is in this limit where we expect signal loss to be greatest, and  $P_{\text{out}}$  becomes:

$$P_{\text{out},\alpha} \approx M_b^\alpha \mathbf{e}^\dagger \mathbf{R}_r \mathbf{Q}^\alpha \mathbf{R}_r \mathbf{e} + 2M_c^\alpha \mathbf{x}^\dagger \mathbf{R}_r \mathbf{Q}^\alpha \mathbf{R}_r \mathbf{e}. \quad (19)$$

The first term of  $P_{\text{out}}$  is simply the weighted power spectrum of  $\mathbf{e}$  alone. Again, it is this quantity that was used in A15 to calculate signal loss. However, without taking into account the cross-terms (the second term), we can substantially under-estimate loss. In short, this is because correlations between the data and injected EoR signal emerge as statistical noise that is added to the power spectrum estimate, decreasing the value of  $P_{\text{out}}$ . Including these cross-terms in our new analysis represents the bulk change of our revised analysis compared to A15.

When  $\mathbf{R}_r$  is taken to be  $\hat{\mathbf{C}}_r^{-1}$ , the second term of Equation (19) is a cross-correlation between  $\hat{\mathbf{C}}_r^{-1} \mathbf{x}$  and  $\hat{\mathbf{C}}_r^{-1} \mathbf{e}$ . As shown in Switzer et al. (2015), this cross-correlation term is non-zero, and in fact negative in expectation. This negative cross-term power arises from a coupling between the inverse of  $\hat{\mathbf{C}}_r$  and  $\mathbf{x}$ . Intuitively, we can see this by expanding the empirical covariance of  $\mathbf{r} = \mathbf{x} + \mathbf{e}$  in the  $|\mathbf{x}| \ll |\mathbf{e}|$  regime:

$$\begin{aligned} \hat{\mathbf{C}}_r &= \langle \mathbf{r} \mathbf{r}^\dagger \rangle_t \\ &= \langle \mathbf{x} \mathbf{x}^\dagger \rangle_t + \langle \mathbf{x} \mathbf{e}^\dagger \rangle_t + \langle \mathbf{e} \mathbf{x}^\dagger \rangle_t + \langle \mathbf{e} \mathbf{e}^\dagger \rangle_t, \end{aligned} \quad (20)$$

where we can neglect the first term because  $\mathbf{x}$  is small. Without loss of generality, we will assume an eigenbasis of  $\mathbf{e}$ , so that  $\langle \mathbf{e} \mathbf{e}^\dagger \rangle_t$  is diagonal. The middle two



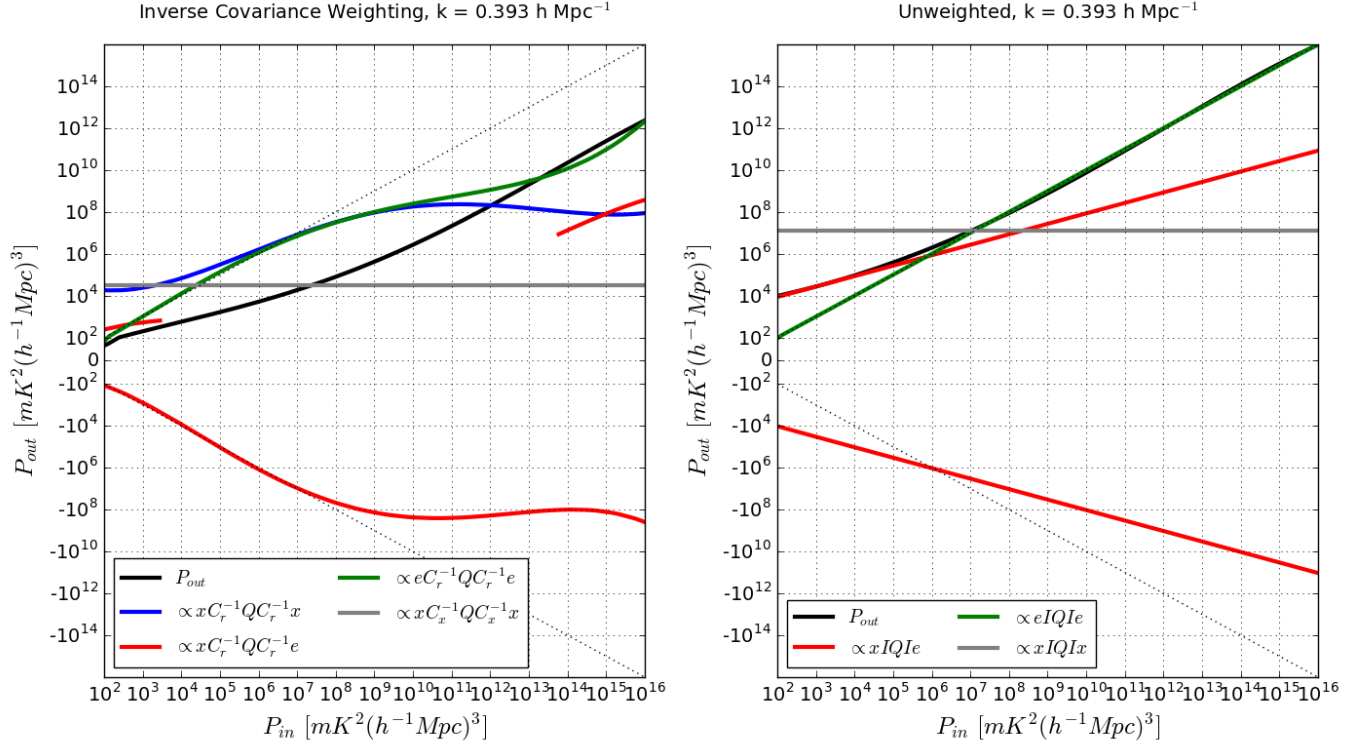


**Figure 17.** Illustration of the components of the signal loss transfer function,  $P_{\text{out}}$ , as defined by Equation (18) for PAPER-64 data for the inverse covariance weighted case (left) and unweighted case (right). The details of the simulation used to generate the figure is explained in Section 3.1.3; here we fit smooth polynomials to our data points to create the curves. We show the contributions of each signal loss term (blue, red, green, gray), which when combined produce the black  $P_{\text{out}}$  curve. Most notably, the green curves denotes the signal loss analysis used in A15, and the red curves showcase the importance of the cross-terms in Equation (18) in computing signal loss. As explained in the main text, the cross-terms can produce large, negative signal which represents the difference between the green curve (which exhibits negligible loss at the data level) and the black curve (which exhibits  $\sim 3$  orders of magnitude of loss at the data level for the inverse variance weighted case). Finally, the dotted diagonal black line represents perfect unity transfer, or no signal loss, which we recover for the unweighted case.

terms, however, can have power in their off-diagonal terms due to the fact that, when averaging over a finite ensemble,  $\langle \mathbf{x} \mathbf{e}^\dagger \rangle_t$  is not zero. As shown in Appendix C of Parsons et al. (2014), to leading order the inversion of a matrix like  $\hat{\mathbf{C}}_r$  that is diagonal-dominant (from  $\langle \mathbf{e} \mathbf{e}^\dagger \rangle_t$ ) with smaller off-diagonal terms results in a new diagonal-dominant matrix with negative off-diagonal terms. These off-diagonal terms depend on both  $\mathbf{x}$  and  $\mathbf{e}$ . When  $\hat{\mathbf{C}}_r^{-1}$  is multiplied into  $\mathbf{x}$ , the result is a vector that is similar to  $\mathbf{x}$  but contains a residual correlation to  $\mathbf{e}$  from the off-diagonal components of  $\hat{\mathbf{C}}_r^{-1}$ . The correlation is negative because the product  $\hat{\mathbf{C}}_r^{-1} \mathbf{x}$  effectively squares the  $\mathbf{x}$ -dependence of the off-diagonal terms in  $\hat{\mathbf{C}}_r^{-1}$  while retaining the negative sign that arose from the inversion of a diagonal-dominant matrix.

The correlation between  $\hat{\mathbf{C}}_r^{-1} \mathbf{e}$  and  $\hat{\mathbf{C}}_r^{-1} \mathbf{x}$  means that we cannot compute signal loss using a signal-only simulation, which would yield greater values for  $P_{\text{out}}$  and thereby underestimate signal loss. Therefore, in our revised signal loss computation we use the full quantity for  $P_{\text{out}}$  as defined in Equation (13), which subtracts the weighted power spectrum of the data from the weighted

power spectrum of data plus EoR.

We thus see from this subsection that signal loss generically arises because of couplings between  $\hat{\mathbf{C}}_r^{-1}$  and  $\mathbf{x}$ . In principle, using  $\hat{\mathbf{C}}_r^{-1}$  in place of the true inverse covariance  $\mathbf{C}^{-1}$  provides yet another source of multiplicative bias, which results in a modification to the treatment shown here. Such a modification is accounted for in the demonstration of Appendix A, where we additionally discard the assumption that  $|\mathbf{x}| \ll |\mathbf{e}|$ . However, despite the loosening of these approximations, one sees that the qualitative message (of anti-correlations resulting in signal loss) remains intact.

### 3.1.3. Signal Loss in Practice

We now shift our attention towards computing signal loss for the fringe-rate filtered PAPER-64 dataset. While our methodology outlined below is independent of weighting scheme, here we demonstrate the computation using inverse covariance weighting ( $\mathbf{R} = \hat{\mathbf{C}}^{-1}$ ), the weighting scheme used in A15 which, with an empirically estimated covariance, leads to substantial loss. With this weighting, our expressions for  $P_{\text{in}}$  and  $P_{\text{out}}$  become:

$$P_{\text{in},\alpha} = M_{\text{in}}^{\alpha} \mathbf{e}^{\dagger} \mathbf{I} \mathbf{Q}^{\alpha} \mathbf{I} \mathbf{e} \quad (21)$$

$$P_{\text{out},\alpha} = M_r^{\alpha} \mathbf{r}^{\dagger} \hat{\mathbf{C}}_r^{-1} \mathbf{Q}^{\alpha} \hat{\mathbf{C}}_r^{-1} \mathbf{r} - M_x^{\alpha} \mathbf{x}^{\dagger} \hat{\mathbf{C}}_x^{-1} \mathbf{Q}^{\alpha} \hat{\mathbf{C}}_x^{-1} \mathbf{x} \quad (22)$$

The treatment we outlined in the previous section implicitly assumed that signal loss corrections could be treated in expectation. In practice, however, the signal loss itself is a random variable — some realizations of the cosmological signal may be more correlated with foreground modes than others, leading to more signal loss. This leads to two issues. The first is that Equation (15) may not hold. In particular, a third term that is a quadratic combination of  $\mathbf{f}$  and  $\mathbf{s}$  (e.g.,  $\mathbf{f}^{\dagger} \mathbf{C}^{-1} \mathbf{s}$ ) may appear. However, we can circumvent this issue by decomposing  $\mathbf{f}$  into a sum of two vectors, one that is proportional to  $\mathbf{s}$  and one that is orthogonal to  $\mathbf{s}$ . The former can be absorbed into the EoR term (part of the signal loss estimate), while the latter can be absorbed into the foreground term. In other words, suppose that we have

$$\hat{\mathbf{p}}_x \approx \ell_{\text{fg}} |\mathbf{f}|^2 + \ell_{\text{eor}} |\mathbf{e}|^2 + \ell_{\text{fe}} \mathbf{f} \cdot \mathbf{e}. \quad (23)$$

in place of Equation (15). Now, split  $\mathbf{f}$  into  $\mathbf{f}_{\parallel} + \mathbf{f}_{\perp}$ , which are the components of the foregrounds that couple to the EoR versus those that do not. Further parameterize  $\mathbf{f}_{\parallel} \equiv \rho \mathbf{e}$ , where  $\rho$  is some correlation coefficient that quantifies the degree of correlation between the foregrounds and the EoR. This then gives

$$\hat{\mathbf{p}}_x \approx \ell_{\text{fg}} |\mathbf{f}|^2 + (\ell_{\text{eor}} + \rho \ell_{\text{fe}}) |\mathbf{e}|^2 + \ell_{\text{fe}} \mathbf{f} \cdot \mathbf{f}_{\perp}. \quad (24)$$

Since  $|\mathbf{e}|^2$  would be a lossless estimate of the true EoR power spectrum, this expression recovers the linear relation between the true EoR power spectrum and the lossy estimate. **[DCJ: Wait what? I think you are saying essentially that some x can remain in Pout which is what we are seeing. Or is this some extra bit of method which has been added to the analysis...]** **[ACL: I'm not sure that's what I'm saying. (And by "I'm not sure" I don't mean it in the colloquial sense of "you're not right and I'm just trying to be polite about it", but rather the literal sense of the phrase "I'm not sure"). What I was trying to say was that if I wrote Equation (15) without the ensemble average, I could say**

$$\hat{\mathbf{p}}_x \approx \ell_{\text{fg}} f^2 + \ell_{\text{eor}} e^2 + \ell_{\text{fe}} f e. \quad (25)$$

**(Note that even this is an approximation. In principle there is an infinite series containing all possible powers of  $e$  and  $f$ ). Now, we split  $f$  into  $f_{\parallel} + f_{\perp}$ , which are the components of the foregrounds that couple to the EoR versus those that do not. Further parameterize  $f_{\parallel} \equiv \rho e$ , where  $\rho$  is some correlation coefficient that quantifies the degree of correlation between the foregrounds and the EoR. Under this parameterization, one can write the  $f e$  term in terms of  $e^2$  (which gets**

**absorbed into the other EoR term, plus residual foregrounds that we don't care about).]** **[ACL: Just promoted this last part to something in the main text.]**

The second issue to tackle is how one incorporates the randomness of  $\ell_{\text{eor}}$  into our signal loss corrections. This is manifest in Equation (24), where the randomness of  $\rho$  means that there is an inherent spread in the signal loss correction. Phrased in the context of Bayes' rule, we wish to find the posterior probability distribution of  $p(\mathbf{p}_{\text{eor}} | \hat{\mathbf{p}}_x)$  for  $\mathbf{p}_{\text{eor}}$  given the uncorrected power spectrum estimate  $\hat{\mathbf{p}}_x$ . Since Equation (17) is a good approximation of Equation (16), which we argued for in the previous section, we can write  $\mathbf{p}_{\text{eor}}$  as  $P_{\text{in}}$ , and hence the probability distribution is given by

$$p(P_{\text{in}} | \hat{\mathbf{p}}_x) \propto \mathcal{L}(\hat{\mathbf{p}}_x | P_{\text{in}}) p(P_{\text{in}}), \quad (26)$$

where  $p(P_{\text{in}})$  is the prior on  $P_{\text{in}}$  and  $\mathcal{L}$  is the likelihood function. Since the likelihood is defined as the distribution of the measured result  $\hat{\mathbf{p}}_x$  given the theoretical power spectrum  $P_{\text{in}}$ , we may construct this function simply by fixing  $P_{\text{in}}$ , and simulating our analysis pipeline for many realizations of the injected EoR signal consistent with this power spectrum. The resulting distribution can be normalized, and the whole process can then be repeated for a different value of  $P_{\text{in}}$ .

In our code, we simulate 20 realizations of  $P_{\text{in}}$  by bootstrapping over baselines, as explained in Section 3.2.2, yielding  $P_{\text{in}}$  values that range from  $\sim 10^2 \text{ mK}^2 (\text{h}^{-1} \text{ Mpc})^3$  to  $\sim 10^{16} \text{ mK}^2 (\text{h}^{-1} \text{ Mpc})^3$ . We also run 25 total EoR injection levels, resulting in a total of 500 data points on our  $P_{\text{in}}$  vs.  $P_{\text{out}}$  grid.

We smooth the 2D distribution of  $P_{\text{in}}$  vs.  $P_{\text{out}}$  using kernel density estimators. The result, for inverse covariance weighting, is shown in the left plot of Figure 18. Bayes' rule then simply instructs us to fix  $\hat{\mathbf{p}}_x$  at our measured value, essentially reading Figure 18 horizontally and reinterpreting Equation (26) as a function of  $p(P_{\text{in}})$ . The final result can then be normalized to give  $p(P_{\text{in}} | \hat{\mathbf{p}}_x)$ . If  $\hat{\mathbf{p}}_x$  itself does not take on a single value but is itself a distribution (for our analysis, this comes from bootstrapping), then one simply repeats the process for every single point on the distribution of  $\hat{\mathbf{p}}_x$ , before performing the final summation and normalization. In Figure 18, the peak of our data distribution  $\hat{\mathbf{p}}_x$  is marked by the solid gray horizontal lines. From the left plot (inverse covariance weighting), one can eyeball that a data value of  $10^5 \text{ mK}^2 (\text{h}^{-1} \text{ Mpc})^3$ , for example, would map approximately to a value of  $\sim 10^8 \text{ mK}^2 (\text{h}^{-1} \text{ Mpc})^3$ , implying a signal loss factor of  $\sim 1000$ . Performing a summation and normalization for the entire distribution of  $\hat{\mathbf{p}}_x$  yields a final  $P_{\text{in}}$  distribution — the distribution of our data as seen through the signal loss lens. We compute power spectrum points from the peak of the histograms, and power spectrum errors from 95% confidence intervals.

As a final complication to our procedure, we note that there will be some intrinsic scatter in our likelihood due

to our having only a finite number of simulations. To separate the intrinsic stochasticity of signal loss from that which arises due to simulation noise, we repeat our analysis for a power spectrum estimator without signal loss ( $\mathbf{R} = \mathbf{I}$ ), shown as the right plot in Figure 18. This intrinsic scatter is shown as the smeared ‘heat-map’ around the solid black diagonal line (representing unity-transfer) in the plot. The width of the lossless scenario’s signal loss likelihood is then deconvolved from the lossy scenario’s signal loss likelihood. Specifically, we deconvolve Gaussian distributions of  $P_{\text{out}}$  in the unweighted case from those of the weighted case (vertical cuts through the plots in Figure 18), for every  $P_{\text{in}}$ . By doing this, we are left with only the intrinsic scatter in signal loss, or scatter that stems from how much the random EoR signal  $\mathbf{e}$  happens to look like the data  $\mathbf{x}$ , a quantity we do not know offhand but one that we would like to correct for. As an extreme example, if we are very unlucky, one realization of  $\mathbf{e}$  would have the same shapes, or eigenvectors, as  $\mathbf{x}$ . An empirically-derived covariance would then down-weight these shapes, destroying the entire EoR signal. On the other hand, the less that  $\mathbf{e}$  looks like  $\mathbf{x}$ , the less signal loss that would result. The intrinsic scatter we can get is not a dominant factor in this case but it is important to correct for the fact that a particular  $P_{\text{out}}$  value could arise from a range of  $P_{\text{in}}$  values.

The shape of our signal loss transfer function can be described as follows. At low injection levels, for small  $\mathbf{e}$ , we are dominated by the cross-terms involving  $\mathbf{e}$  and  $\mathbf{x}$  in Equation (19). As  $\mathbf{e}$  increases, we move into a regime where  $P_{\text{out}} \sim P_{\text{in}}$ , and then eventually into a regime where  $P_{\text{out}} < P_{\text{in}}$  when  $\mathbf{e}$  is large enough to be destroyed if weighting the data using itself. Although we only show figures for one  $k$  value, we note that the shape of the transfer curve is nearly identical for all  $k$ ’s (though we treat each  $k$  separately).

To conclude this method, we also show power spectrum results for fringe-rate filtered PAPER-64 data before and after signal loss estimation in Figure 19, using inverse covariance weighting. The blue dashed line represents the unweighted power spectrum  $2\sigma$  upper limit, which is identical in both panels (an important check, as we expect no signal loss for this case). The black and gray points are positive and negative power spectrum values plotted with  $2\sigma$  error bars. Prior to signal loss estimation, it is clear that the power spectrum is unfeasible because it is well below the theoretical noise level prediction (solid green curve). Post-estimation, the power spectrum errors blow up to be higher than both the theory and unweighted power spectrum, a consequence of not being able to characterize covariances well using the time-averaged fringe-rate filtered data (there is less independent information to use). We elaborate on this point in the next section, as well as investigate alternate weighting schemes to inverse covariance weighting, with the goal of finding one that balances the aggressiveness of down-weighting contaminants with minimizing

the loss of EoR signal.

#### 3.1.4. Minimizing Signal Loss

With a signal loss formalism established, we now have the capability of experimenting with different weighting options for  $\mathbf{R}$ . Our goal here is to choose a weighting method that successfully down-weights foregrounds and systematics in our data without generating large amounts of signal loss. We have found that the balance between the two is a delicate one and requires a careful understanding and altering of covariance matrices.

We saw in Section 2.1.3 how limiting the number of down-weighted eigenmodes (i.e. flattening out part of the eigenspectrum) can help minimize signal loss. We experiment with this idea on PAPER-64 data, dialing the number of modes that are down-weighted from zero (which is equivalent to identity-weighting, or the unweighted case) to 21 (which is full inverse covariance weighting of our 21 channels). The power spectrum results for one  $k$  value, both before and after signal loss estimation, are shown in the top panel in Figure 20. We see that the amount of signal loss increases as weighting becomes more aggressive (gray curve). In other words, more ‘weak’ (EoR-dominated) fluctuations are being overfit and subtracted as more modes are down-weighted. We also find that the power spectrum upper limit, post signal loss estimation, increases with the number of down-weighted modes (black curve). Because our data is fringe-rate filtered, we have less information to characterize the covariance matrix and therefore do a worse job estimating it. Hence, the more modes we use in down-weighting, the greater the error we have in estimating the power spectrum.

Optimistically, we expect there to be a ‘sweet spot’ as we dial our regularization knob; a level of regularization where weighting is beneficial compared to not weighting (blue dashed line). In other words, we would like a weighting scheme that down-weights eigenmodes that predominantly describe foreground modes, but not EoR modes. We see in Figure 20 that this occurs when only the strongest  $\sim 3$ -4 eigenmodes are down-weighted, though the improvement from the unweighted case is small.

We also saw in Section 2.1.3 how adding the identity matrix to the empirical covariance can minimize signal loss. We experiment with this idea as well, shown in the bottom panel of Figure 20. The grey and black lines represent power spectrum limits pre and post signal loss estimation, respectively, as a function of the strength of  $\mathbf{I}$  that is added to  $\hat{\mathbf{C}}$ , quantified as the percentage of the  $\text{Tr}(\hat{\mathbf{C}})$  added to  $\hat{\mathbf{C}}$ . When 0% of the  $\text{Tr}(\hat{\mathbf{C}})$  is used, it is equivalent to full inverse covariance weighting. From this plot we see that only a small percentage of  $\text{Tr}(\hat{\mathbf{C}})$  is needed to significantly reduce loss. We expect that as the strength of  $\mathbf{I}$  is increased (going to the left), both the black and gray curves will approach the unweighted case.

In addition to our thermal noise prediction (green) and

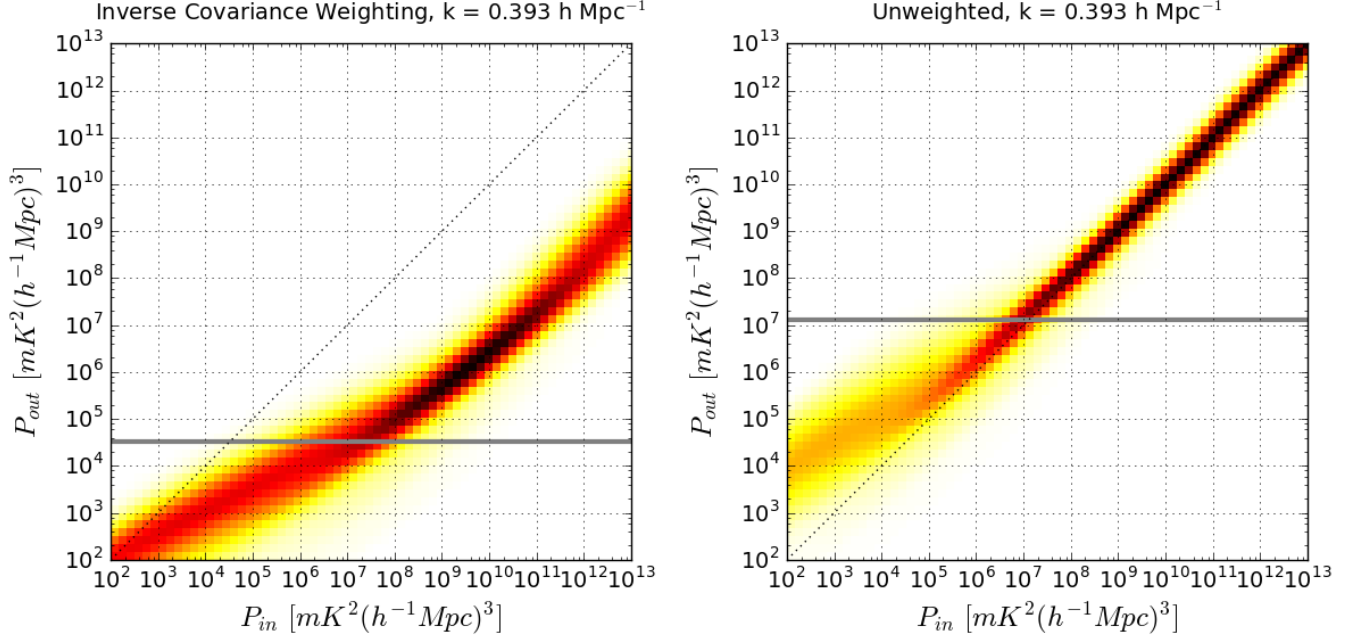


**Figure 18.** Signal loss transfer functions showing the relationship of  $P_{in}$  and  $P_{out}$ , as defined by Equations (12) and (13). Kernel density estimations of the power spectrum transfer functions are shown as colored heat-maps for the cases of inverse covariance weighted PAPER-64 data (left) and unweighted data (right). The solid black diagonal line marks a perfect unity mapping, and the solid gray horizontal line denotes the power spectrum value of the data  $\hat{P}_x$ . From these plots, it is clear that inverse covariance weighting results in  $\sim 3$  orders of magnitude of signal loss for power spectrum values above  $\sim 2 \times 10^4 mK^2(h^{-1} \text{ Mpc})^3$ , whereas the unweighted case does not exhibit loss. The peculiar ‘signal gain’ tail seen at low injection is driven by the cross-terms in Equation (19), also shown by the red curve in the right panel in Figure 17.

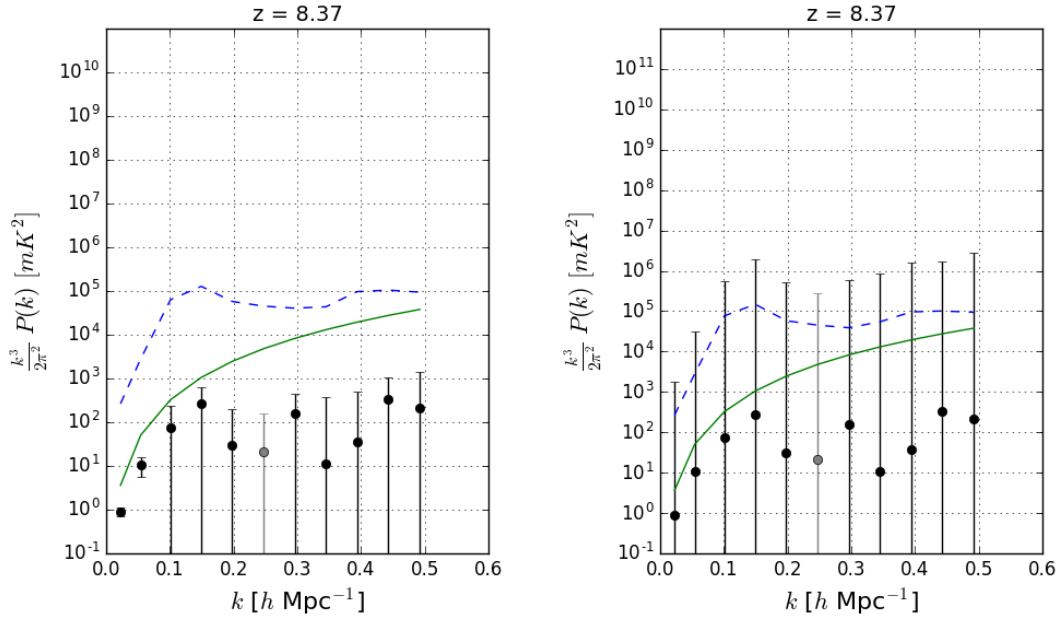


**Figure 19.** Full inverse covariance weighted power spectrum of PAPER-64 data (positive points in black and negative points in gray, with  $2\sigma$  error bars) before signal loss estimation (left) and after (right). The dashed blue line is the unweighted power spectrum ( $2\sigma$  upper limit). The solid green line is the theoretical  $2\sigma$  noise level prediction based on observational parameters, whose calculation is detailed in Section 3.2.1.



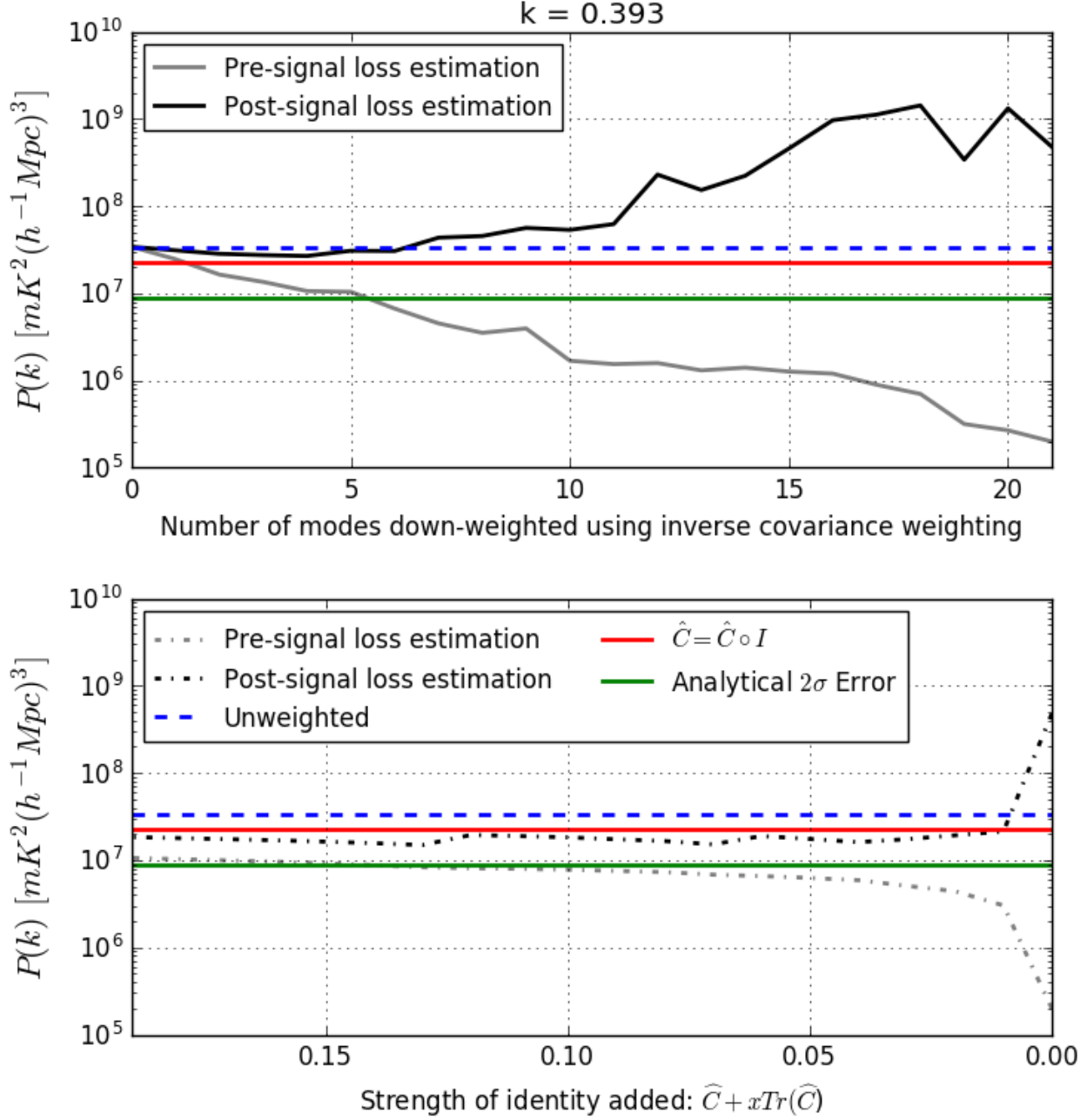


**Figure 20.** Power spectra  $2\sigma$  upper limits for  $k = 0.393 \text{ h Mpc}^{-1}$  for fringe-rate filtered PAPER-64 data. Top: Values are shown before (gray) and after (black) signal loss estimation as a function of number of eigenmodes of  $\hat{\mathbf{C}}$  that are down-weighted. This regularization knob is tuned from 0 modes on the left (i.e. unweighted) to 21 modes on the right (i.e. full inverse covariance weighting). Over  $\sim 3$  orders of magnitude of signal loss results when using inverse covariance weighting. Bottom: Power spectrum upper limits before (gray) and after (black) signal loss estimation as a function of identity added to the empirical covariance. This regularization knob is tuned from 0% of the  $\text{Tr}(\hat{\mathbf{C}})$  added to  $\hat{\mathbf{C}}$  on the right (i.e. full inverse covariance weighting) to 20% of  $\text{Tr}(\hat{\mathbf{C}})$  added to  $\hat{\mathbf{C}}$  on the left. Also plotted in both panels for comparison are  $2\sigma$  power spectrum upper limits for the unweighted case (dashed blue) and inverse variance weighted case (red); both are after signal loss estimation. Finally, a theoretical prediction for noise ( $2\sigma$  error) is plotted as solid green. In the revised PAPER-64 analysis in this paper, we choose to use a regularization scheme of  $\hat{\mathbf{C}} \equiv 0.04\text{Tr}(\hat{\mathbf{C}}) + \hat{\mathbf{C}}$  because it outperforms both the down-weighting individual eigenmodes and inverse variance cases.

unweighted power spectrum limit (blue), one additional horizontal line is shown in Figure 20 in both panels and represents a third regularization technique. This line (red) denotes the power spectrum value, post-signal loss estimation, for inverse variance weighting (multiplying an identity matrix element-wise to  $\hat{\mathbf{C}}$ ). This result is single-valued and not a function of the x-axes. We see that all three regularization schemes shown (black solid, black dashed, red) perform similarly at their best (i.e. when  $\sim 3\text{--}4$  eigenmodes are down-weighted in the case of the black solid curve). However, for the remainder of this paper, we choose to use the weighting option of  $\hat{\mathbf{C}} \equiv \hat{\mathbf{C}} + 0.04\text{Tr}(\hat{\mathbf{C}})$ , which we will denote as  $\hat{\mathbf{C}}_{eff}$ . We choose this weighting scheme because it slightly out-performs the other weighting schemes, likely due to the fact that it retains information from all eigenmodes (i.e. it doesn't throw away some information as in the other cases) but re-weights them in a way that produces minimal loss.

Our revised, best to-date PAPER-64 power spectrum (using only one baseline separation type and  $\hat{\mathbf{C}}_{eff}$ ) is shown in Figure 21. Again, black and gray points correspond to positive and negative power spectrum values respectively, with  $2\sigma$  errors bars. Also plotted are the unweighted power spectrum upper limit (dashed blue) and theoretical prediction of noise (solid green). From this result, we quote a best  $2\sigma$  upper limit of  $(151.0 \text{ mK})^2$  at  $k = 0.34 \text{ hMpc}^{-1}$ , a higher limit than A15 by a factor of  $\sim 7$  in mK (though we only use one baseline type in our analysis as opposed to three). **[CC: replace with kolopanis limit instead later]**

In this section we have shown three simple ways of regularizing  $\hat{\mathbf{C}}$  to minimize signal loss using PAPER-64 data. There are many other weighting schemes that we leave for consideration in future work. For example, one could estimate  $\hat{\mathbf{C}}$  using information from different subsets of baselines. For redundant arrays this could mean calculating  $\hat{\mathbf{C}}$  from a different but similar baseline type, such as the  $\sim 30 \text{ m}$  diagonal PAPER baselines (instead of the horizontal E/W ones). Alternately, covariances could be estimated from all other baselines except the two being cross-multiplied when forming a power spectrum estimate. This method was used in Parsons et al. (2014) (a similar method was also used in Dillon et al. (2015)) in order to avoid suppressing the 21 cm signal, and it's worth noting that the PAPER-32 results are likely less impacted from the issue of signal loss underestimation because of this very reason (however, they are affected by the error estimation issues described in Section 3.2, so we also regard those results as suspect and superseded by those of Kolopanis et al., *in prep*).

Another possible way to regularize  $\hat{\mathbf{C}}$  is to use information from different ranges of LST. For example, one could calculate  $\hat{\mathbf{C}}$  with data from LSTs where foregrounds are stronger (earlier or later LSTs than the 'foreground-quiet' range used in forming power spectra) — doing so may yield a better description of the foregrounds that we desire to down-weight, especially if

residual foreground chromaticity is instrumental in origin and stable in time. Fundamentally, each of these examples are similar in that they rely on a computation of  $\hat{\mathbf{C}}$  from data that is similar but not exactly the same as the data that is being down-weighted. Ideally this would be effective in down-weighting shared contaminants yet avoid signal loss from over-fitting EoR modes in the power spectrum dataset itself.

### 3.2. PAPER-64: Error Estimation

In this section we discuss the ways in which we estimate errors for PAPER-64 power spectra. We first walk through a derivation for a theoretical error estimation (of thermal noise) based on observational parameters. Although a theoretical model often differs from true errors as explained in Section 2.2, it is helpful to understand the ideal case and the factors that affect its sensitivity. Additionally, we build on the lessons learned about bootstrapping in Section 2.2 to revise our bootstrapping method as applied to PAPER-64 data in order to compute accurate errors from the data itself.

In particular, we highlight major changes in both our sensitivity calculation and bootstrapping method that differ from the A15 analysis of PAPER-64. While we do not discuss the changes within the context of PAPER-32, it is worth noting that the power spectrum results in Parsons et al. (2014) are affected by the same issues.

#### 3.2.1. Theoretical Error Estimation

Re-analysis of the PAPER-64 data included a detailed study using several independently generated noise simulations. What we found was that these simulations all agreed but were discrepant with the previous analytic sensitivity calculations. The analytic calculation is only an approximation, however the differences were large enough (factors of 10 in some cases) to warrant a careful investigation. The analytic calculation attempts to combine a large number of pieces of information in an approximate way, and when re-considering some of the approximations, we have found there to be large effects. What follows here is an accounting of the differences which have been discovered.

The sensitivity prediction (Parsons et al. 2012a; Pober et al. 2013) for a power spectral analysis of interferometric 21 cm data, in temperature-units, is:

$$p(k) = \frac{X^2 Y \Omega_{eff} T_{sys}^2}{\sqrt{2 N_{lst} N_{seps} t_{int} N_{days} N_{bls} N_{pols}}} \quad (27)$$

- $X^2 Y$ : Conversion factors from observing coordinates (angles on the sky and frequency) to cosmological coordinates (co-moving distances). For  $z = 8.4$ ,  $X^2 Y = 5 \times 10^{11} h^{-3} \text{ Mpc}^3 \text{ str}^{-1} \text{ GHz}^{-1}$ .
- $\Omega_{eff}$ : The effective primary beam area in steradians (Parsons et al. 2010; Pober et al. 2012). The effective beam area changes with the application of a fringe-rate filter, since different parts of the

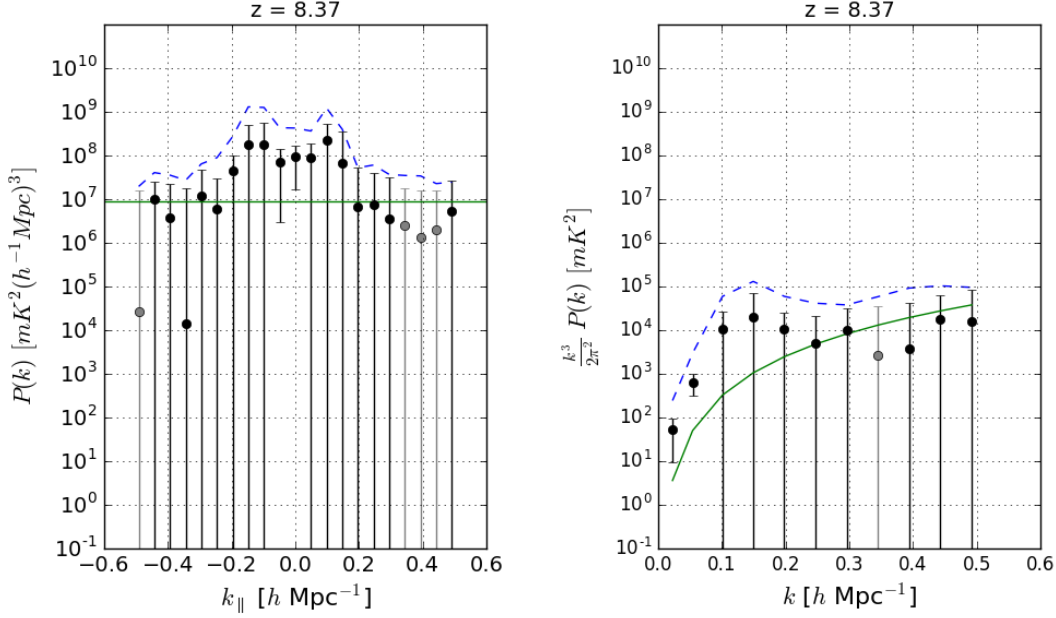


**Figure 21.** Power spectrum of PAPER-64 using  $\hat{\mathbf{C}}_{eff}$ . Black and gray points correspond to positive and negative power spectrum values, respectively, with  $2\sigma$  error bars also plotted. The dashed blue line is the unweighted power spectrum ( $2\sigma$  upper limit). The solid green line is the theoretical  $2\sigma$  noise level prediction based on observational parameters. This power spectrum result differs from A15 in that it only uses data from one type of baseline (30 m East/West baselines) instead of three. Major differences from previously published results stem from revisions regarding signal loss, bootstrapping, and the theoretical error computation. From this, we quote a best  $2\sigma$  upper limit of  $(151.0 \text{ mK})^2$  at  $k = 0.34 \text{ hMpc}^{-1}$ , a higher limit than A15 by a factor of  $\sim 7$  in mK [CC: replace with kolopanis limit later].

beam are up-weighted and down-weighted. Using numbers from Table 1 in Parsons et al. (2016),  $\Omega_{eff} = 0.74^2/0.24$  for an optimal fringe-rate filter.

- $T_{sys}$ : The system temperature is set by:

$$T_{sys} = 180 \left( \frac{\nu}{0.18} \right)^{-2.55} + T_{rcvr}, \quad (28)$$

where  $\nu$  are frequencies in GHz. We use a receiver temperature of 144 K, yielding  $T_{sys} = 431 \text{ K}$  at 150 MHz. This is lower than the  $T_{sys}$  of 500 K used in A15 because of several small miscalculation errors that were identified<sup>2</sup>.

- $\sqrt{2}$ : This factor in the denominator of the sensitivity equation comes from taking the real part of the power spectrum estimates after cross-multiplying independent ‘even’ and ‘odd’ visibility measurements (which is done principally to avoid a noise bias). In A15, a factor of 2 was mistakenly used.
- $N_{lst}$ : The number of LST bins that go into a power spectrum estimation. The sensitivity scales as the square root because we integrate incoherently over time. For PAPER-64,  $N_{lst} = 8$ .

- $N_{seps}$ : The number of baseline separation types averaged incoherently in a final power spectrum estimate. For the analysis in this paper, we only use one type of baseline, hence  $N_{seps} = 1$ . The updated limits in Kolopanis et al., *in prep* use three separation types.

- $t_{int}$ : Length of an independent integration of the data. It is crucial to adapt this number if filtering is applied along the time axis (i.e. a fringe-rate filter). We compute the effective integration time of our fringe-rate filtered data by scaling the original integration time  $t_i$  using the following:

$$t_{int} = t_i \frac{\int 1 df}{\int w^2(f) df}, \quad (29)$$

where  $t_i = 43$  seconds,  $t_{int}$  is the fringe-rate filtered integration time,  $w$  is the fringe-rate profile, and the integral is taken over all fringe-rates. For PAPER-64, this number is  $t_{int} = 3857 \text{ s}$ .

- $N_{days}$ : The total number of days of data analyzed. In A15, this number was set to 135. However, because we divide our data in half (to form ‘even’ and ‘odd’ datasets), this number should be reduced by a factor of 2. Additionally, because our LST coverage is not 100% complete (it doesn’t overlap for every single day), we compute a more realistic value

<sup>2</sup> For example, there was a missing a square root in going from a variance to a standard deviation.

of  $N_{days}$  as:

$$\frac{1}{N_{days}} = \sqrt{\left\langle \frac{1}{N_i^2} \right\rangle_i}, \quad (30)$$

where  $i$  is over LST (Jacobs et al. 2015). For PAPER-64, our revised estimate of  $N_{days}$  is  $\sim 34$  days.

- $N_{bls}$ : The number of baselines contributing to the sensitivity of a power spectrum estimate. In A15, this number was the total number of 30 m East/West baselines used in the analysis. However, using the total number of baselines neglects the fact that baselines are averaged into groups (see Section 3.2.2) for computational speed-up when cross-multiplying data. Our revised estimate for the parameter is:

$$N_{bls} = \frac{N_{bls}}{N_{gps}} \sqrt{N_{gps}^2 - N_{gps}}, \quad (31)$$

where, for the A15 analysis,  $N_{gps} = 5$ . Each baseline group averages down linearly as the number of baselines entering the group ( $N_{bls}/N_{gps}$ ) and then as the square root of the number of cross-multiplied pairs ( $\sqrt{N_{gps}^2 - N_{gps}}$ ). For the revised PAPER-64 analysis with only one baseline separation type, this becomes  $N_{bls} \sim 46$  instead of 51.

- $N_{pols}$ : The number of polarizations averaged together. For the case of Stokes I,  $N_{pols} = 2$ .

An additional factor of  $\sqrt{2}$  is gained in sensitivity when folding our power spectra into  $\Delta^2(k)$ , due to averaging together positive and negative  $k$ 's.

Our revised sensitivity estimate for PAPER-64 is shown in comparison with that of A15 in Figure 22. Together, the revised parameters yield a decrease in sensitivity (higher noise floor) by a factor of  $\sim 5$  in  $\text{mK}^2$ .

To verify our thermal noise prediction, we form power spectra estimates using a pure noise simulation. We create Gaussian random noise assuming a constant  $T_{rcvr}$  (translated into  $T_{sys}$  via Equation (28)) but accounting for the true  $N_{days}$  as determined by LST sampling counts for each time and frequency in the LST-binned data. We convert  $T_{sys}$  into a variance statistic using:

$$T_{rms} = \frac{T_{sys}}{\sqrt{\Delta\nu\Delta t N_{days} N_{pols}}}, \quad (32)$$

where  $\Delta\nu$  is channel spacing,  $\Delta t$  is integration time,  $N_{days}$  is the number of daily counts for a particular time and frequency that went into our LST-binned set, and  $N_{pols}$  is the number of polarizations (2 for Stokes I). This RMS temperature sets the variance of the Gaussian random noise.

Power spectrum results for the noise simulation, which uses our full power spectrum pipeline, are shown in Figure 23, where the black and gray points represent positive and negative power spectrum values, respectively

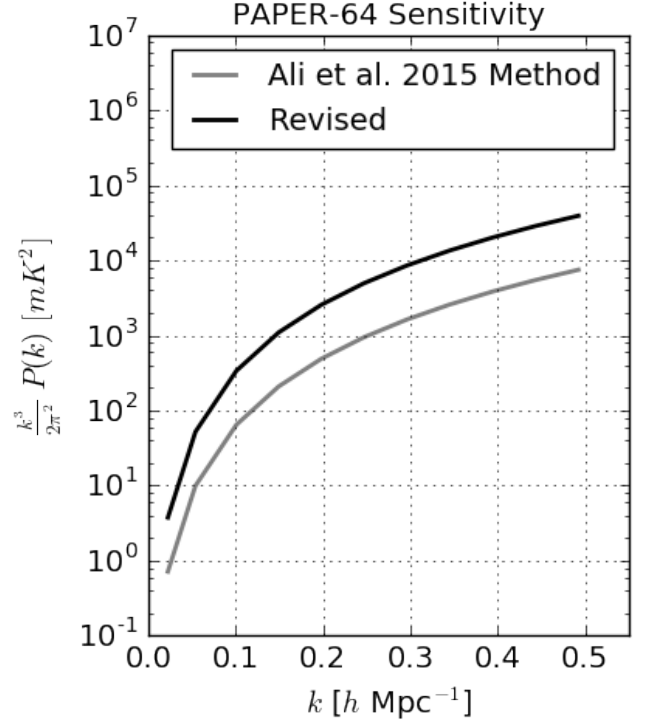


**Figure 22.** An updated prediction for the noise-level of PAPER-64 data (black) is shown in comparison to previously published sensitivity limits (gray). Both sensitivity analyses plotted assume only one baseline type (an additional factor of  $\sqrt{3}$  for three baseline types is needed to match A15 exactly). Major factors that contribute to the discrepancy are  $\Omega_{eff}$ ,  $N_{days}$  and  $N_{bls}$ , as in Equation (27) and described in Section 3.2.1, which when combined decreases our sensitivity (higher noise floor) by a factor of  $\sim 5$  in  $\text{mK}^2$ .

(with  $2\sigma$  error bars and weighting matrix  $\hat{C}_{eff}$ ), the dashed blue line represents the unweighted power spectrum, and the solid green line denotes our  $2\sigma$  theoretical noise prediction as calculated by Equation (27). All three are in agreement, validating our analytical thermal noise calculation.

### 3.2.2. Bootstrapping

We bootstrap PAPER-64 power spectra in order to determine confidence intervals for our results. In this section, we highlight one major changes in the way we estimate errors since A15, using the lesson we've learned about bootstrapping independent samples.

As discussed in Section 2.2, bootstrapping is only a valid way of estimating errors if a dataset is comprised of independent samples, or the number of independent samples is well known. The PAPER-64 pipeline outputs 20 bootstraps (over baselines), each a 2-dimensional power spectrum that is a function of  $k$  and time.

In A15, a second round of bootstrapping occurred over the time axis. A total of 400 bootstraps were created in this step ( $N_{boot} = 400$ ), each comprised of randomly selected values sampled with replacement along the time axis. More specifically, each of these bootstraps contained the same number of values as the number of time



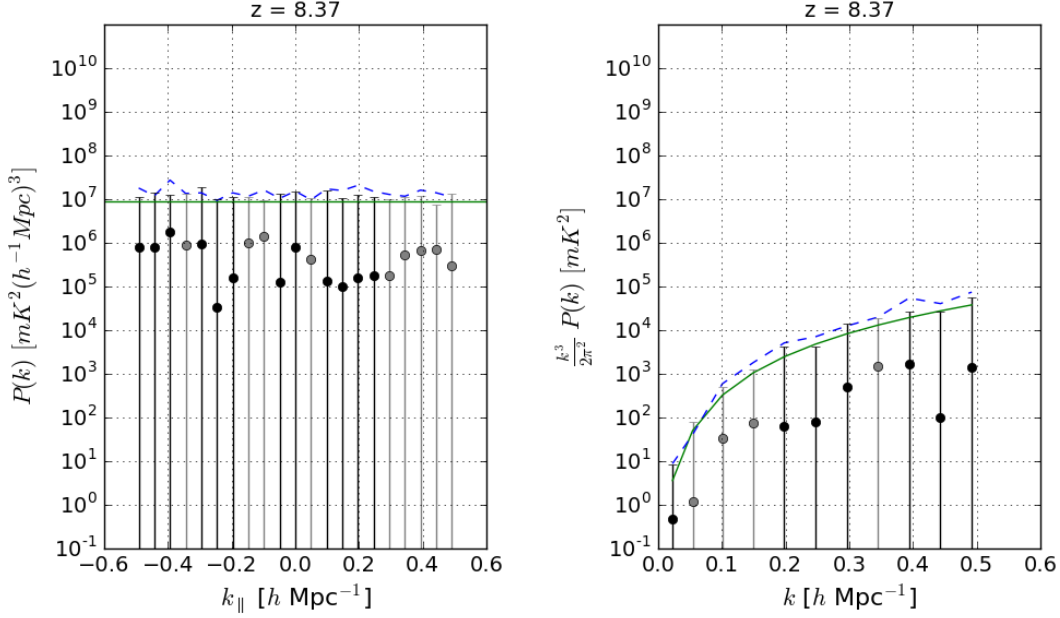


**Figure 23.** Power spectrum estimate for a noise simulation that mimics the noise level of PAPER-64 data. The weighted power spectrum points and their  $2\sigma$  errors are shown in black and gray (positive and negative values), where we use  $\hat{\mathbf{C}}_{eff}$  to minimize signal loss. The dashed blue line is the unweighted power spectrum (also  $2\sigma$  upper limit). The solid green line is the theoretical  $2\sigma$  noise level prediction as calculated by Equation (27). All three estimates agree (the analytic curve should encompass 95% of the points).

integrations (which, at  $\sim 700$ , greatly exceeds the approximate number of independent samples after fringe-rate filtering). Medians were then taken of the values in each bootstrap (with the appropriate median correction factor applied). Finally, power spectrum limits were computed by taking the mean and standard deviation over all the bootstraps. We emphasize again that in this previous analysis, the number of elements sampled per bootstrap greatly exceeded the number of independent LST samples, under-estimating errors. A random draw of 700 measurements from this dataset has many repeated values, and the variance between hundreds ( $N_{boot}$ ) of these random samples is smaller than the true underlying variance of the data.

Given our new understanding of the sensitivity of bootstraps to the number of elements sampled, we have removed the second bootstrapping step along time entirely and now simply bootstrap over baselines. Power spectrum estimates with this bootstrapping change for fringe-rate filtered noise are shown in Figure 24. The estimates are unweighted in order to disentangle the effects of bootstrapping from signal loss. As shown in the figure, when more elements are drawn for each bootstrap than the number of independent samples (by over-sampling elements along the time axis), repeated values begin to crop up and the apparent variation between bootstraps drops, resulting in limits (gray) below the predicted noise level (green). Using the revised bootstrapping method, where bootstrapping only occurs over the baseline axis, the errors (black) are shown to agree with the analytic.

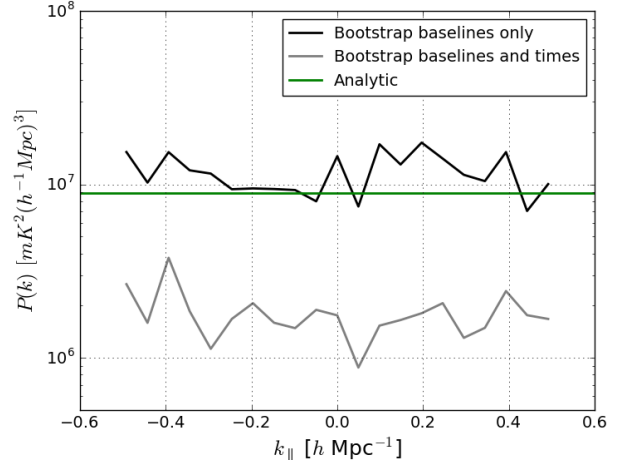


**Figure 24.**  $2\sigma$  power spectrum errors (not upper limits) for a noise simulation (computed via Equation (32) using PAPER-64 observing parameters) using two different bootstrapping methods. The noise is fringe-rate filtered and a weighting matrix of  $\mathbf{I}$  (unweighted) is used in order to disentangle the effects of bootstrapping from signal loss. The bootstrapping method used in A15 is shown in gray, where bootstrapping occurs along both the baseline and time axes. This under-estimates errors by sampling more values than independent ones in the dataset (fringe-rate filtering reduces the number of independent samples along time). We use the method illustrated by the black curve in our updated analysis, where bootstrapping only occurs along the baseline axis. This is shown to agree with the  $2\sigma$  analytic prediction for noise (green).

### 3.3. PAPER-64: Bias

In Section 2.3 we highlighted some common sources of bias that can show up as power spectrum detections and imitate EoR. We discussed the importance of using jackknife and null tests for instilling confidence in an EoR detection, as well as identifying other sources of biases. Here we demonstrate methods used by PAPER-64 to mitigate foreground and noise bias and we perform null tests in order to characterize the stability and implications of our results.

#### 3.3.1. Mitigating Bias

We briefly discuss one way we mitigate foreground leakage in a power spectrum estimate, and two ways we suppress noise biases. These methods are not novel to this analysis but here we frame them in the context of minimizing false (non-EoR) detections.

Tailoring window functions is one way to suppress foreground biases. As alluded to in Section 2.1, we have a choice for the normalization matrix  $\mathbf{M}$  in Equation (2). For the analysis of PAPER-64 data, we compute  $\mathbf{M}$  using the Fisher matrix  $\mathbf{F}$ , defined as:

$$\mathbf{F}_{\alpha\beta} = \frac{1}{2} \text{tr}[\mathbf{R}\mathbf{Q}^\alpha \mathbf{R}\mathbf{Q}^\beta] \quad (33)$$

where  $\mathbf{R}$  is the data-weighting matrix and  $\alpha$  and  $\beta$  are wavebands in  $k_\parallel$ . We take the Cholesky decomposition of  $\mathbf{F}$ , decomposing it into two lower triangular matrices (which is possible since  $\mathbf{F}$  is Hermitian):

$$\mathbf{F} = \mathbf{L}\mathbf{L}^\dagger. \quad (34)$$

Next, we construct  $\mathbf{M}$ :

$$\mathbf{M} = \mathbf{D}\mathbf{L}^{-1} \quad (35)$$

where  $\mathbf{D}$  is a diagonal matrix. In doing so, our window function, defined as  $\mathbf{W} = \mathbf{M}\mathbf{F}$ , becomes:

$$\mathbf{W} = \mathbf{D}\mathbf{L}^\dagger. \quad (36)$$

Because of the nature of the lower triangular matrix, this window function has the property of preventing the leakage of foreground power from low  $k$  to high  $k$  modes. Specifically, we order the elements in  $\mathbf{F}$  in such a way so that power can leak from high  $k$  modes to low  $k$  modes, but not vice versa. Since most foreground power shows up at low  $k$ 's, this method ensures a window function that retains clean, noise-dominated measurements while minimizing the contamination of foreground bias. This tailored window function was used in the A15 analysis, however for this paper, we use  $\mathbf{M} \propto \mathbf{I}$  for simplicity.

In addition to mitigating foreground bias at high  $k$ 's, two other sources of bias that we actively suppress in the PAPER-64 analysis are noise bias associated with the squaring of thermal noise and noise bias from crosstalk. In order to avoid the former, we filter out certain cross-multiplications when forming  $\hat{q}$  in Equation (1). Namely, the PAPER-64 dataset is divided into

two halves: even julian dates and odd julian dates. Our data vectors are then  $\mathbf{x}_{\text{even},1}$  for the ‘even’ dataset and baseline group 1,  $\mathbf{x}_{\text{odd},1}$  for the ‘odd’ dataset and baseline group 1, etc. We only form  $\hat{q}$  when the two copies of  $\mathbf{x}$  come from different groups and baselines, never multiplying ‘even’ with ‘even’, for example, in order to prevent the squaring of the same thermal noise. We recognize that this method results in a hit to our sensitivity. Sensitivity can be gained, for example, by only dividing up the dataset once (either along time or baselines), or by creating more groups (more cross-multiplications), but in this paper we only attempt to revise the A15 analysis (which uses the same groupings), not produce the most sensitive limits of PAPER-64.

To mitigate crosstalk bias, which appears as a static bias in time, we apply a fringe-rate filter that suppresses fringe-rates of zero. Figure 16 shows that the filter response is zero for such static signals. The effect of filtering out zero fringe-rates on power spectrum results is shown in A15. Most notably, power spectrum detections exist at all  $k$ 's without crosstalk removal and these are detections that, depending on the power spectrum level, could be mistaken for EoR.

#### 3.3.2. Jackknife Tests

The highest sensitivity power spectrum result for PAPER-64 using the updated analysis presented in this paper, shown in Figure 21, has positive biases at low  $k$  values. As discussed in Section 2.3.1, these detections are most likely attributable to foreground leakage. Here we demonstrate three null tests performed on PAPER-64 data that verify that the positive detections are indeed due to foreground variation and not attributable to EoR.

The three null test results are shown in Figure 25, with each test described as the following:

- Original Data (black): This is identical to the unweighted, revised PAPER-64 power spectrum in Figure 21 (one baseline type only) with weighting matrix  $\mathbf{I}$ . There are clear detections at low  $k$ 's.
- Even/Odd (blue): We split our dataset into even (e) and odd (o) days, where  $\mathbf{x}_1 = e + o$  and  $\mathbf{x}_2 = e - o$ . We form datasets in this way to ensure that we use the full sensitivity of our data. When cross-multiplied, we obtain:

$$\mathbf{x}_1 \mathbf{x}_2^\dagger = ee^\dagger - eo^\dagger + oe^\dagger - oo^\dagger \quad (37)$$

If the same sky signal is in both the even and odd datasets, we expect it to cancel out.

- Baselines (green): We split our dataset into two halves, where each contains half of the total baselines used in the analysis. Again, we form  $\mathbf{x}_1 = b_1 + b_2$  and  $\mathbf{x}_2 = b_1 - b_2$ , where  $b_1$  is the first baseline group and  $b_2$  is the second baseline group.
- LST (magenta): We split our dataset into two halves based on LST, namely  $t_1$  (LSTs 0.5-4.6

hours) and  $t_2$  (LSTs 4.6-8.6 hours). We form our two datasets as  $\mathbf{x}_1 = t_1 + t_2$  and  $\mathbf{x}_2 = t_1 - t_2$ .

Investigating Figure 25, we find that none of the null tests are fully consistent with noise; we would expect the null tests' error bars to be contained within the gray shaded region (theoretical error) for a 'passable' test. We note, however, that the error bars for the baselines test (green) and even/odd test (blue) are smaller than those of the LST test (magenta).

This suggests that the primary systematic driving our power spectrum points and errors to be outside the estimated error region is LST-dependent, and therefore likely to be residual foregrounds. In other words,  $t_1$  and  $t_2$  differ by an amount greater than thermal noise and they do not effectively cancel out the sky signal during cross-multiplication. While residual foregrounds are the primary cause for power spectrum results above the theoretical noise (as in Figure 21), other unexplained variations exist which are present in all the null tests. These variations could be attributable to... **[CC: fill in]**

We do not investigate the detailed nature of the residual foregrounds in this paper, though one could imagine performing many similar null tests with a sliding window of  $t_1$ 's and  $t_2$ 's. This would illuminate the particular LST range that introduces the foreground bias (or whether the bias is constant in LST), and could potentially be traced to an individual bright radio source. This type of detailed analysis will be critical at EoR sensitivities, however, for our current analysis we are not surprised that the main source of bias we see comes from foregrounds in regions where we expect leakage.

#### 4. CONCLUSION

Although current 21 cm published power spectrum upper limits lie several orders of magnitude above predicted EoR levels, ongoing analyses of deeper sensitivity datasets from PAPER, MWA, and LOFAR, as well as next generation instruments like HERA, are expected to continue to push towards EoR sensitivities. As the field progresses towards a detection, we have shown that it is crucial for future analyses to have a rigorous understanding of signal loss in an analysis pipeline, be able to accurately and robustly calculate both power spectrum and theoretical errors, and consistently undergo a comprehensive set of jackknife and null tests.

In particular, in this paper we have investigated the subtleties and tradeoffs of common 21 cm power spectrum techniques on signal loss, error estimation, and bias, which can be summarized as follows:

- Substantial signal loss can result when weighting data using empirically estimated covariances (Section 2.1). Loss of the 21 cm signal is especially significant the fewer number of independent modes that exist in the data. Hence, there exists a trade-off between sensitivity driven time-averaging techniques such as fringe-rate filtering and signal loss when using empirically estimated covariances.

- Signal injection and recovery simulations can be used to quantify signal loss (Section 3.1). However, a signal-only simulation (i.e. comparing an unweighted vs. weighted power spectrum of EoR only) can underestimate loss by failing to account for correlations between the data and signal (Section 3.1.2).
- Errors that are estimated via bootstrapping can be underestimated if samples in the dataset are significantly correlated (Section 2.2). If the number of independent samples in a dataset is well-determined, bootstrapping is a simple and accurate way of estimating errors.
- Meaningful null tests are vital to validate an EoR detection (Section 2.3.2). Similarly, performing jackknife tests along multiple axes of a dataset is necessary for confidence in an EoR detection and can also be used to tease out systematics.

As a consequence of our investigations, we have also revised power spectrum results from PAPER-64. For an analysis of only one baseline type, we quote a new  $2\sigma$  upper limit of  $(151.0 \text{ mK})^2$  at  $k = 0.34 \text{ hMpc}^{-1}$ , a higher limit than A15 by a factor of  $\sim 7$  in mK **[CC: replace with kolopanis limit later]**. The reasons for a previously underestimated limit and ways in which our new analysis differs can be summarized by the following:

- Signal loss, previously found to be  $< 2\%$  in A15, was under-estimated by a factor of  $\sim 1000$  for inverse covariance weighting. For our new analysis, we use a regularized covariance weighting method to minimize loss (Section 3.1.4). However, because our revised weighting method is not as aggressive as the former, our results are still a factor of  $\sim 7$  in mK higher than previous limits. Under-estimated signal loss therefore represents the bulk of our revision. We note that PAPER's analysis is not the first to under-estimate loss; results from the GMRT (Paciga et al. 2013) were also revised from new signal loss calculations associated with their singular value decomposition foreground filter.
- Power spectrum errors, originally computed by bootstrapping, were under-estimated by a factor of  $\sim 1.4$  in mK due to oversampling data whose effective number of independent samples was reduced from fringe-rate filtering (Section 3.2.2).
- Several factors used in an analytic expression to predict the noise-level in PAPER-64 data were revised, yielding a decrease in predicted sensitivity level by a factor of  $\sim 2$  in mK (Section 3.2.1). We have verified our revised prediction extensively using pure noise simulations. We note that our sensitivity prediction is revised by a factor less than our power spectrum result, implying that if taken at face value, the theoretical prediction for noise in A15 was too high for its data points.

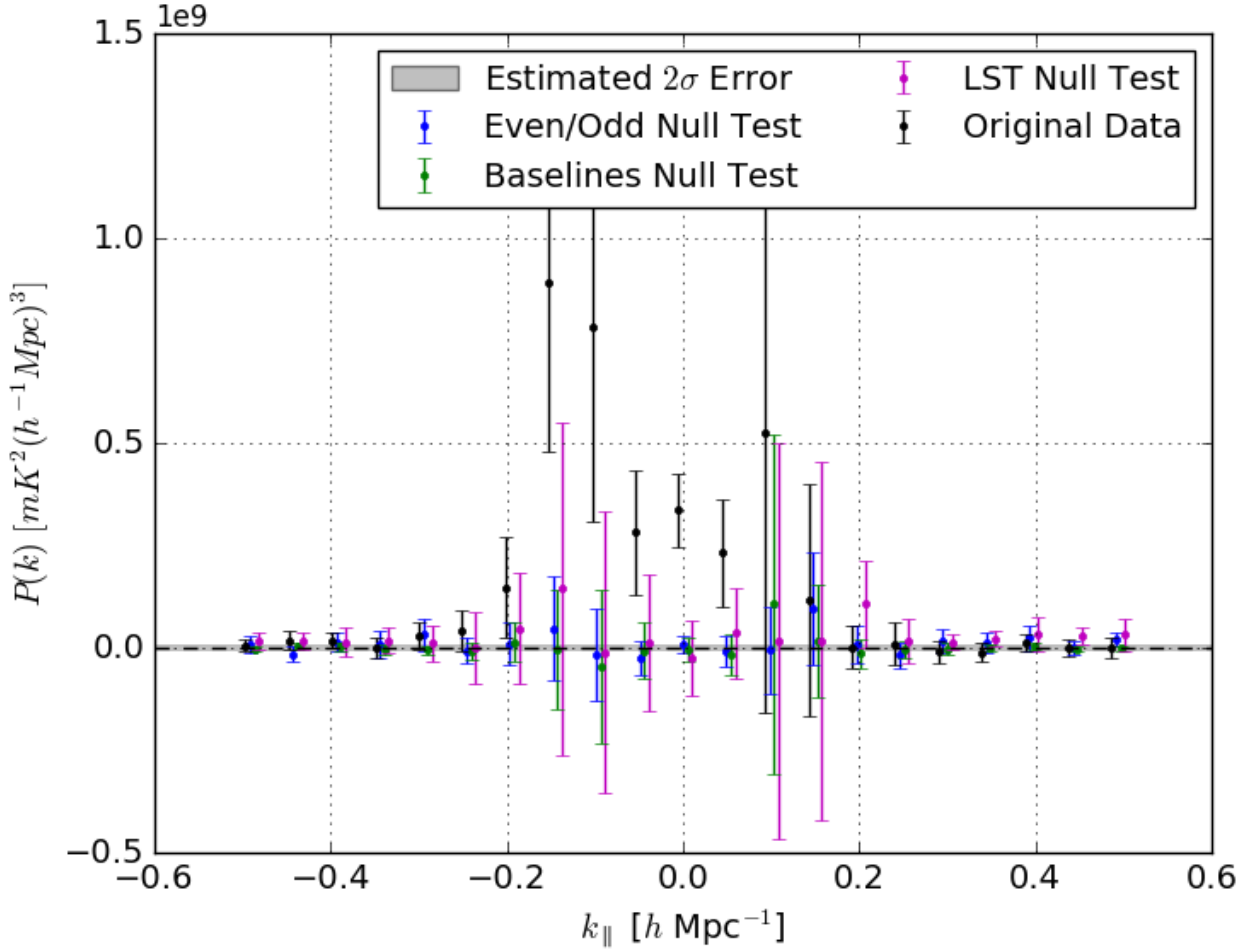


**Figure 25.** Results for three null tests compared to the PAPER-64 unweighted revised power spectrum (black) and analytically estimated  $2\sigma$  errors (gray shaded region). For each, we take a jackknife along a different axis of the dataset - along julian days (separating even and odd days; blue), along baselines (green), and along LST (magenta). We expect the sky signal to disappear for a ‘passing’ null test (for all error bars to be contained to within the gray shaded region). We find that none of the null tests performed pass, and that the dominant source of the biases in our power spectrum are likely caused by variation of foregrounds in LST (due to the magenta result being the most inconsistent with noise)

The future of 21 cm cosmology is exciting, as new experiments have sensitivities that expect to reach and surpass EoR levels, improved foreground mitigation/removal strategies are being developed, and simulations are being designed to better understand instruments. On the power spectrum analysis side, robust signal loss simulations, precise error calculations, and comprehensive jackknife tests will play critical roles in accurate 21 cm results. With strong foundations being established now, it is safe to say that we can expect to learn much about reionization and our early Universe in the coming years.

## 5. ACKNOWLEDGEMENTS

CC would like to acknowledge the UC Berkeley Chancellor’s Fellowship, National Science Foundation Graduate Research Fellowship (Division of Graduate Education award 1106400), and thank Eric Switzer for helpful discussions. PAPER and HERA are supported by grants from the National Science Foundation (awards 1440343, and 1636646). ARP, DCJ, and JEA would also like to acknowledge NSF support (awards 1352519, 1401708, and 1455151, respectively). SAK is supported by the University of Pennsylvania School of Arts and Sciences Dissertation Completion Fellowship. JSD acknowledges NSF AAPF award 1701536. We graciously thank SKA-SA for site infrastructure and observing support.

## APPENDIX

### A. A TOY MODEL FOR SIGNAL LOSS

In this Appendix, we examine a toy model for signal loss. Our goal is to derive an analytic formula for power spectrum signal loss. We will also show that in general, signal loss appears as a multiplicative bias on one’s power



spectrum estimate.

The minimum-variance quadratic estimator  $\hat{p}_\alpha$  for the  $\alpha$ th bandpower of the power spectrum is given by

$$\hat{p}_\alpha = \frac{1}{2\mathbf{F}_{\alpha\alpha}} \mathbf{x}^t \mathbf{C}^{-1} \mathbf{Q}^\alpha \mathbf{C}^{-1} \mathbf{x}, \quad (\text{A1})$$

where

$$F_{\alpha\alpha} \equiv \frac{1}{2} \text{tr} (\mathbf{C}^{-1} \mathbf{Q}^\alpha \mathbf{C}^{-1} \mathbf{Q}^\alpha) \quad (\text{A2})$$

is the  $\alpha$ th diagonal element of the Fisher matrix (for this section only, with no loss of generality, we assume that the data  $\mathbf{x}$  are real). In our case, however, we do not have *a priori* knowledge of the covariance matrix. Thus, we replace  $\mathbf{C}$  with  $\hat{\mathbf{C}}$ , its data-derived approximation. Our estimator then becomes

$$\hat{p}_\alpha^{\text{loss}} = \frac{1}{2\hat{\mathbf{F}}_{\alpha\alpha}} \mathbf{x}^t \hat{\mathbf{C}}^{-1} \mathbf{Q}^\alpha \hat{\mathbf{C}}^{-1} \mathbf{x}, \quad (\text{A3})$$

where

$$\hat{F}_{\alpha\alpha} \equiv \frac{1}{2} \text{tr} (\hat{\mathbf{C}}^{-1} \mathbf{Q}^\alpha \hat{\mathbf{C}}^{-1} \mathbf{Q}^\alpha), \quad (\text{A4})$$

with the label “loss” to foreshadow the fact that this will be an estimator with signal loss (i.e., a multiplicative bias of less than unity). We will now provide an explicit demonstration of this by modeling the estimated covariance as

$$\hat{\mathbf{C}} = (1 - \eta) \mathbf{C} + \eta \mathbf{x} \mathbf{x}^t, \quad (\text{A5})$$

where  $\eta$  is a parameter quantifying our success at estimating the true covariance matrix. If  $\eta = 0$ , our covariance estimate has perfectly modeled the true covariance and  $\hat{\mathbf{C}} = \mathbf{C}$ . On the other hand, if  $\eta = 1$ , then our covariance estimate is based purely on the one realization of the covariance that is our actual data, and we would expect a high level of overfitting and signal loss.

Our strategy for computing the signal loss will be to insert Equation (A5) into Equation (A3) and to express the resulting estimator  $\hat{p}_\alpha^{\text{loss}}$  in terms of  $\hat{p}_\alpha$ . We begin by expressing  $\hat{\mathbf{C}}^{-1}$  in terms of  $\mathbf{C}^{-1}$  using the Woodbury identity so that

$$\hat{\mathbf{C}}^{-1} = \frac{\mathbf{C}^{-1}}{1 - \eta} \left[ \mathbf{I} - \frac{\eta \mathbf{x} \mathbf{x}^t \mathbf{C}^{-1}}{1 + \eta(g - 1)} \right], \quad (\text{A6})$$

where we have defined  $g \equiv \mathbf{x}^t \mathbf{C}^{-1} \mathbf{x}$ . Inserting this into our Fisher estimate we have

$$\hat{F}_{\alpha\alpha} = \frac{F_{\alpha\alpha}}{(1 - \eta)^2} \left[ 1 - \frac{\eta}{1 + \eta(g - 1)} \frac{h_{\alpha\alpha}}{F_{\alpha\alpha}} + \frac{1}{2} \left( \frac{\eta}{1 + \eta(g - 1)} \right)^2 \frac{h_\alpha^2}{F_{\alpha\alpha}} \right], \quad (\text{A7})$$

where  $h_\alpha \equiv \mathbf{x}^t \mathbf{C}^{-1} \mathbf{Q}^\alpha \mathbf{C}^{-1} \mathbf{x}$  and  $h_{\alpha\alpha} \equiv \mathbf{x}^t \mathbf{C}^{-1} \mathbf{Q}^\alpha \mathbf{C}^{-1} \mathbf{Q}^\alpha \mathbf{C}^{-1} \mathbf{x}$ . Note that  $g$ ,  $h_\alpha$ , and  $h_{\alpha\alpha}$  are all random variables, since they depend on  $\mathbf{x}$ . Inserting these expressions into our estimator gives

$$\hat{p}_\alpha^{\text{loss}} = \frac{1}{2} \frac{h_\alpha}{F_{\alpha\alpha}} \left[ 1 - \frac{\eta g}{1 + \eta(g - 1)} \right]^2 \left[ 1 - \frac{\eta}{1 + \eta(g - 1)} \frac{h_{\alpha\alpha}}{F_{\alpha\alpha}} + \frac{1}{2} \left( \frac{\eta}{1 + \eta(g - 1)} \right)^2 \frac{h_\alpha^2}{F_{\alpha\alpha}} \right]^{-1}. \quad (\text{A8})$$

Both for the purposes of analytical tractability and to provide intuition, we expand this expression to leading order in  $\eta$ . The result is

$$\hat{p}_\alpha^{\text{loss}} \approx \frac{1}{2} \frac{h_\alpha}{F_{\alpha\alpha}} \left[ 1 - \eta \left( g - \frac{h_{\alpha\alpha}}{F_{\alpha\alpha}} \right) \right]. \quad (\text{A9})$$

Taking the ensemble average of both sides and noting that the true power spectrum  $p_\alpha$  is equal to  $\langle h_\alpha \rangle / 2F_{\alpha\alpha}$ , we obtain

$$\langle \hat{p}_\alpha^{\text{loss}} \rangle \approx (1 - \eta N) p_\alpha + 4\eta \frac{\text{tr}(\mathbf{C}^{-1} \mathbf{Q}^\alpha \mathbf{C}^{-1} \mathbf{Q}^\alpha \mathbf{C}^{-1} \mathbf{Q}^\alpha)}{[\text{tr}(\mathbf{C}^{-1} \mathbf{Q}^\alpha \mathbf{C}^{-1} \mathbf{Q}^\alpha)]^2} \approx (1 - \eta N) p_\alpha, \quad (\text{A10})$$

where  $N$  is the length of  $\mathbf{x}$ . In the last step we dropped the final term, since it scales as  $\eta p_\alpha$  (without the factor of  $N$ ) and is therefore typically small compared to the terms that have been retained. Now, recall that  $p_\alpha$  is the *true* power spectrum. This means that it can be decomposed into the sum of the foreground and EoR power spectra, since the foregrounds and EoR are uncorrelated in expectation. This toy example, while not definitive, serves to motivate the form of Equation (15).

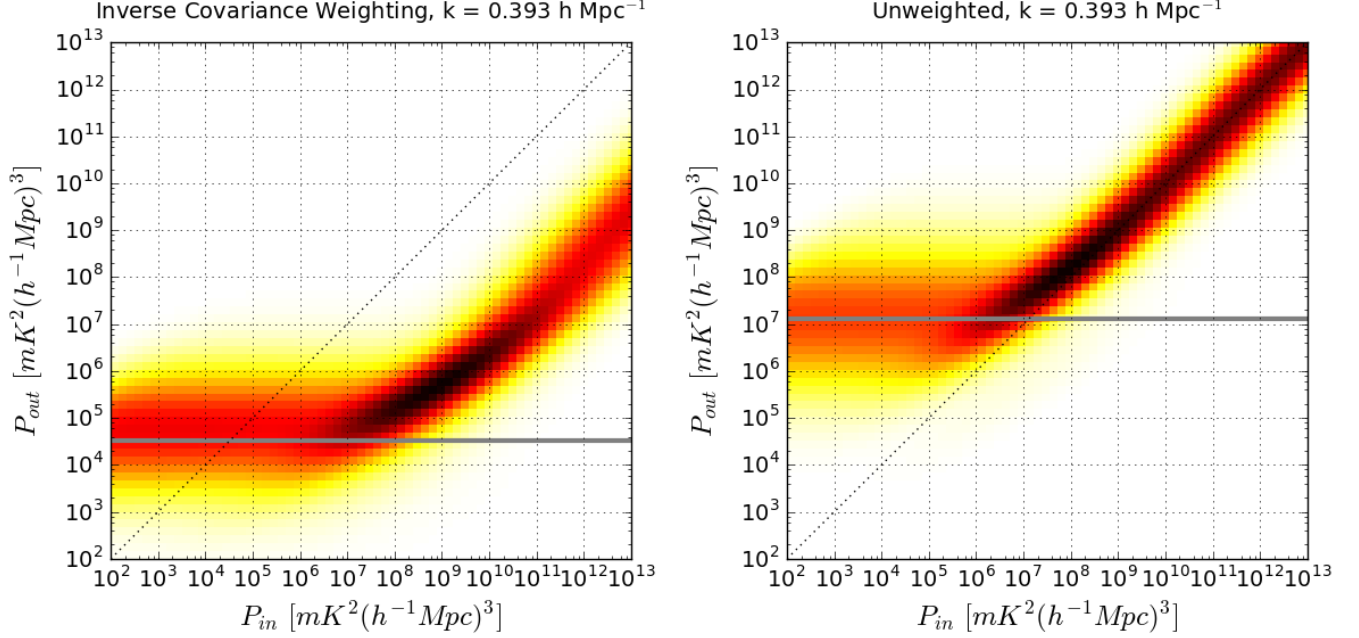


**Figure B1.** The distribution of output power spectrum values for a given injection level  $P_{in}$ . The  $P_{out}$  values that are plotted on the y-axis represent the weighted power spectrum of data plus the injected signal. It differs from that of Figure 18 by not subtracting off the power spectrum of data alone (not subtracting off the second term in Equation (13)). We show kernel density estimations of the power spectrum transfer functions as colored heat-maps for the cases of inverse covariance weighted PAPER-64 data (left) and unweighted data (right). The solid black diagonal line marks a perfect unity mapping, and the solid gray horizontal line denotes the peak of  $\hat{\mathbf{p}}_x$ , the data distribution. At low injection,  $P_{out}$  converges to the data level. [JCP: This figure needs updating (as does this caption). The text seems to have settled on  $P_{out}$  referring to  $\hat{\mathbf{p}}_r - \hat{\mathbf{p}}_x$ , whereas this signal loss methodology uses only  $\hat{\mathbf{p}}_r$ . So the y-axis needs to change.]

## B. SIMPLIFIED LOSS CORRECTION

One of the main difficulties in defining a signal loss procedure is in the interpretation of the injection procedure ‘output’. The method described in Section 3.1 relies on several assumptions which required justification including the neglect of cross-terms in the power spectrum and indeed does not behave as expected at small injected values. However it is possible to make a simpler interpretation which requires less motivation.

In the main text we made an estimate of the signal loss effecting only the injected EoR by supposing that the lossy injected signal was the difference between the injected and not injected cases:  $P_{out} = \hat{\mathbf{p}}_r - \hat{\mathbf{p}}_x$ . Suppose that we rephrase the question we are asking to: “At what point would an injected signal be detectable at significant levels?”. Instead of disentangling the part of the output power spectrum dominated by the injected signal we can simply use  $\hat{\mathbf{p}}_r$ , the weighted power spectrum of the data plus injected signal.

This question is phrased visually in Figure B1. In the 2D space relating total  $\hat{\mathbf{p}}_r$  to injected  $P_{in}$ , very small injected levels begin at the level equivalent of no injection (i.e. data only) and very large levels are dominated by the injected signal. It is the transition zone, where the injected signal amplitude is similar to the data level (and thus subject to cross correlations in both the covariance and in the power spectrum calculation) that we search for the point at which an injected signal would be clearly detected.

One difference in this method from the one in the main text is that we are exclusively asking about signals detectable *above* the level of the observed data. Thus it is explicitly limited to placing an upper limit, even if in some  $k$ -modes one has actual detections above the noise. This might be seen as more conservative, however, a similar assumption has already been made when choosing to down-weight the data using itself. In such a down-weighting step, one has assumed that significant excess power is associated with a foreground residual. We note that a high SNR detection will require a different method.

Formally we can express our test as: “What is the  $P_{in}$  such that

$$\hat{\mathbf{p}}_r > \hat{\mathbf{p}}_x \Lambda, \quad (\text{B11})$$

where  $\Lambda$  represents a choice of threshold?” Of course, both sides of this equation are actually a distribution of values associated with data variance and injected model variance. One way to interpret this test for the two distributions is

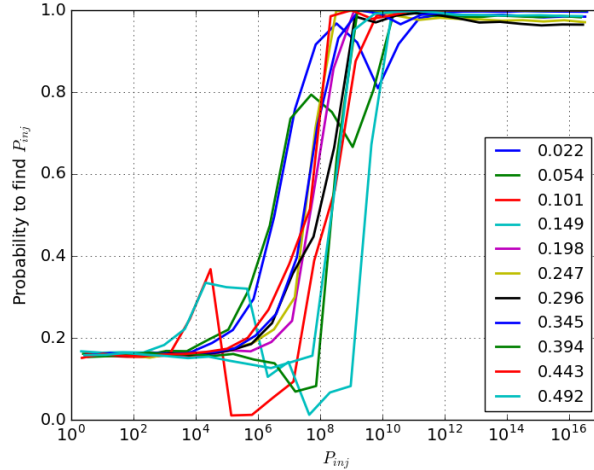


**Figure B2.** The probability that an injected signal of level  $P_{inj}$  is observable at a  $2\sigma$  level above the value of  $\hat{\mathbf{p}}_x$  (data). The different colors represent different  $k$  values. We choose a probability of 95% for our signal loss estimated power spectrum.

to compute the probability that the two distributions are not (i.e. the null test) the same.

$$\mathbf{P}(P_{in}) = 1 - \int_{r=x} \mathbf{P}(\hat{\mathbf{p}}_x) \mathbf{P}(\hat{\mathbf{p}}_r, P_{in}) dr \quad (\text{B12})$$

where  $\mathbf{P}(\hat{\mathbf{p}}_x)$  is the probability of obtaining the power spectrum  $\hat{\mathbf{p}}_x$  found via bootstrapping (power spectrum of data only) and  $\mathbf{P}(\hat{\mathbf{p}}_r, P_{in})$  is the probability of obtaining the summed power spectrum  $\hat{\mathbf{p}}_r$  given a range of input power levels, as sampled in Figure B1.

Probability vs. injection level is shown in Figure B2. At low injection levels the variation between  $\mathbf{x}$  and  $\mathbf{r}$  is such that the null test is ruled out to within 20%. This is the level expected from two distributions with  $\sim 10$  effective samples. As the injected signal approaches the level of the data, the probability of null rejection rises steeply.

Lastly, this method requires that we choose the probability at which we choose to reject the null hypothesis. As can be seen in Figure B2, the difference between 80% and 90% can mean a difference of almost an order of magnitude in the power spectrum level that is ruled out. We can also see that, due to the small number of samples, the probability does not perfectly converge at high injected power levels. Rather than insist on a rejection at the 99th percent level, we compromise at 95%.

The resulting limits for inverse covariance weighted PAPER-64 data (the same data used in Section 3.1, no regularization), using this second signal loss method, are shown in Figure B3 compared with the method used in the main text. Overall the limits show good agreement, with  $k$  modes differing by factors of  $\sim 3$ .

## REFERENCES

- Ade, P., et al. 2008, *Astrophysical Journal*, 674, 22
- Ade, P. A. R., et al. 2017, *PhRvD*, 96, 102003
- Ali, S. S., Bharadwaj, S., & Chengalur, J. N. 2008, *MNRAS*, 385, 2166
- Ali, Z. S., et al. 2015, *ApJ*, 809, 61
- Andrae, R. 2010, *ArXiv e-prints*
- Beardsley, A. P., et al. 2016, *The Astrophysical Journal*, 833, 102
- Bernardi, G., et al. 2009, *A&A*, 500, 965
- . 2010, *A&A*, 522, A67+
- Bernardi, G., et al. 2016, *Monthly Notices of the Royal Astronomical Society*, 461, 2847
- Bond, J. R., Jaffe, A. H., & Knox, L. 1998, *PhRvD*, 57, 2117
- Bowman, J. D., & Rogers, A. E. E. 2010, *Nature*, 468, 796
- Burns, J. O., et al. 2012, *Advances in Space Research*, 49, 433
- Chiang, H. C., et al. 2010, *The Astrophysical Journal*, 711, 1123
- Crites, A. T., et al. 2015, *The Astrophysical Journal*, 805, 36
- Das, S., et al. 2011, *Physical Review Letters*, 107, 021301
- Datta, A., Bowman, J. D., & Carilli, C. L. 2010, *The Astrophysical Journal*, 724, 526
- de Oliveira-Costa, A., Tegmark, M., Gaensler, B. M., Jonas, J., Landecker, T. L., & Reich, P. 2008, *MNRAS*, 388, 247
- DeBoer, D. R., et al. 2017, *Publications of the Astronomical Society of the Pacific*, 129, 045001
- Dillon, J. S., Liu, A., & Tegmark, M. 2013, *PhRvD*, 87, 043005
- Dillon, J. S., et al. 2014, *Phys. Rev. D*, 89, 023002
- . 2015, *Phys. Rev. D*, 91, 123011
- Dodelson, S., & Schneider, M. D. 2013, *PhRvD*, 88, 063537
- Ewall-Wice, A., Dillon, J. S., Liu, A., & Hewitt, J. 2017, *MNRAS*, 470, 1849
- Furlanetto, S. R., Oh, S. P., & Briggs, F. H. 2006, *PhR*, 433, 181
- Ghosh, A., Bharadwaj, S., Ali, S. S., & Chengalur, J. N. 2011, *MNRAS*, 418, 2584
- Hartlap, J., Simon, P., & Schneider, P. 2007, *A&A*, 464, 399
- Jacobs, D. C., et al. 2015, *ApJ*, 801, 51
- Jelić, V., et al. 2008, *MNRAS*, 389, 1319
- Joachimi, B. 2017, *MNRAS*, 466, L83

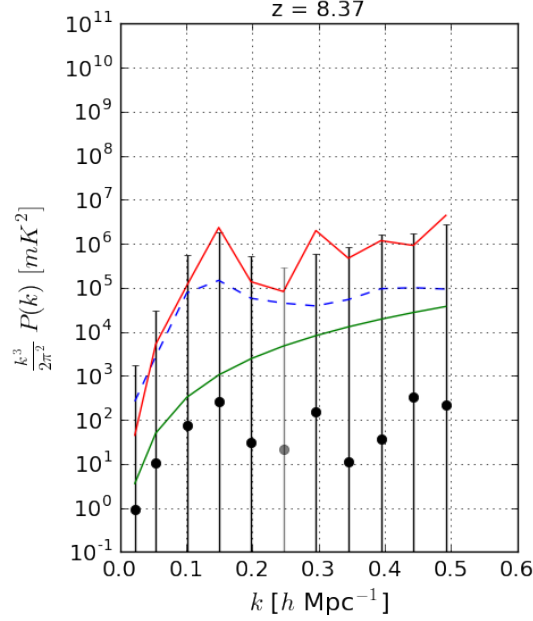


**Figure B3.** A comparison of the signal loss method described in Section 3.1 with the method in this appendix at 95% confidence (red curve). Also shown are the upper limits of the unweighted power spectrum (blue dashed) and theoretical noise model (green).

Keating, G. K., Marrone, D. P., Bower, G. C., Leitch, E., Carlstrom, J. E., & DeBoer, D. R. 2016, *The Astrophysical Journal*, 830, 34

Keck Collaboration, A., et al. 2016, 833

Kohn, S. A., et al. 2016, *ApJ*, 823, 88

Liu, A., & Parsons, A. R. 2016, *Monthly Notices of the Royal Astronomical Society*, 457, 1864

Liu, A., Parsons, A. R., & Trott, C. M. 2014a, *PhRvD*, 90, 023018

—. 2014b, *PhRvD*, 90, 023019

Liu, A., & Tegmark, M. 2011, *Phys. Rev. D*, 83, 103006

Moore, D. F., Aguirre, J. E., Parsons, A. R., Jacobs, D. C., & Pober, J. C. 2013, *The Astrophysical Journal*, 769, 154

Morales, M. F., & Wyithe, J. S. B. 2010, *ARA&A*, 48, 127

Paciga, G., et al. 2013, *MNRAS*

Padmanabhan, N., White, M., Zhou, H. H., & O’Connell, R. 2016, *MNRAS*, 460, 1567

Parsons, A., Pober, J., McQuinn, M., Jacobs, D., & Aguirre, J. 2012a, *ApJ*, 753, 81

Parsons, A. R., Liu, A., Ali, Z. S., & Cheng, C. 2016, *ApJ*, 820, 51

Parsons, A. R., Pober, J. C., Aguirre, J. E., Carilli, C. L., Jacobs, D. C., & Moore, D. F. 2012b, *ApJ*, 756, 165

Parsons, A. R., et al. 2010, *AJ*, 139, 1468

—. 2014, *ApJ*, 788, 106

Patil, A. H., et al. 2017, *ApJ*, 838, 65

Patra, N., Subrahmanyan, R., Sethi, S., Udaya Shankar, N., & Raghunathan, A. 2015, *ApJ*, 801, 138

Paz, D. J., & Sánchez, A. G. 2015, *MNRAS*, 454, 4326

Pearson, D. W., & Samushia, L. 2016, *MNRAS*, 457, 993

Peterson, U.-L. P. X.-P. W. J. 2004, *ArXiv Astrophysics e-prints*

Petrovic, N., & Oh, S. P. 2011, *MNRAS*, 413, 2103

Pober, J. C., et al. 2012, *The Astrophysical Journal*, 143, 53

Pober, J. C., et al. 2013, *AJ*, 145, 65

—. 2014, *ApJ*, 782, 66

Pober, J. C., et al. 2016, *The Astrophysical Journal*, 819, 8

Pope, A. C., & Szapudi, I. 2008, *MNRAS*, 389, 766

Pritchard, J. R., & Loeb, A. 2012, *Reports on Progress in Physics*, 75, 086901

QUIET, Q., et al. 2011, *The Astrophysical Journal*, 741, 111

—. 2012, *The Astrophysical Journal*, 760, 145

Santos, M. G., Cooray, A., & Knox, L. 2005, *ApJ*, 625, 575

Sellentin, E., & Heavens, A. F. 2016, *MNRAS*, 456, L132

Sherwin, B. D., et al. 2017, *Phys. Rev. D*, 95, 123529

Sokolowski, M., et al. 2015, *PASA*, 32, e004

Switzer, E. R., Chang, T.-C., Masui, K. W., Pen, U.-L., & Voytek, T. C. 2015, *The Astrophysical Journal*, 815, 51

Taylor, A., & Joachimi, B. 2014, *MNRAS*, 442, 2728

Tegmark, M. 1997, *PhRvD*, 55, 5895

Thyagarajan, N., et al. 2013, *ApJ*, 776, 6

Tingay, S. J., et al. 2013, *PASA*, 30, 7

Trott, C. M., Wayth, R. B., & Tingay, S. J. 2012, *ApJ*, 757, 101

Trott, C. M., et al. 2016, *The Astrophysical Journal*, 818, 139

van Haarlem, M. P., et al. 2013, *A&A*, 556, A2

Vedantham, H., Shankar, N. U., & Subrahmanyan, R. 2012, *The Astrophysical Journal*, 745, 176

Voytek, T. C., Natarajan, A., Jáuregui García, J. M., Peterson, J. B., & López-Cruz, O. 2014, *ApJL*, 782, L9

Wang, J., et al. 2013, *The Astrophysical Journal*, 763, 90

Wu, X. 2009, in *Bulletin of the American Astronomical Society*, Vol. 41, American Astronomical Society Meeting Abstracts #213, 474